Bioactive Materials 6 (2021) 2767–2782

Contents lists available at ScienceDirect

Bioactive Materials

journal homepage: www.sciencedirect.com/journal/bioactive-materials

Three-dimensional decellularized tumor extracellular matrices with different stiffness as bioengineered tumor scaffolds

Yonggang Lv [a,b,*,1], Hongjun Wang [a,b], Gui Li [a,b], Boyuan Zhao [a,b]

[a] Mechanobiology and Regenerative Medicine Laboratory, Bioengineering College, Chongqing University, Chongqing, 400044, PR China
[b] Key Laboratory of Biorheological Science and Technology, Chongqing University, Ministry of Education, Bioengineering College, Chongqing University, Chongqing, 400044, PR China

ARTICLE INFO

Keywords:
Breast tumor cell
Decellularized scaffold
Lysyl oxidase
Extracellular matrix
Matrix stiffness
Drug resistance

ABSTRACT

In the three-dimensional (3D) tumor microenvironment, matrix stiffness is associated with the regulation of tumor cells behaviors. *In vitro* tumor models with appropriate matrix stiffness are urgently desired. Herein, we prepare 3D decellularized extracellular matrix (DECM) scaffolds with different stiffness to mimic the microenvironment of human breast tumor tissue, especially the matrix stiffness, components and structure of ECM. Furthermore, the effects of matrix stiffness on the drug resistance of human breast cancer cells are explored with these developed scaffolds as case studies. Our results confirm that DECM scaffolds with diverse stiffness can be generated by tumor cells with different lysyl oxidase (LOX) expression levels, while the barely intact structure and major components of the ECM are maintained without cells. This versatile 3D tumor model with suitable stiffness can be used as a bioengineered tumor scaffold to investigate the role of the microenvironment in tumor progression and to screen drugs prior to clinical use to a certain extent.

1. Introduction

Breast cancer that occurs in the mammary gland epithelium is the most prevalent malignant tumor in women worldwide. During cancer progression and metastasis, malignant cells maintain their close interactions with surrounding cells and the extracellular matrix (ECM). Numerous stromal cells, soluble factors, signal molecules and ECM collectively constitute the complex three-dimensional (3D) tumor microenvironment that possesses several properties, such as an acidic pH, low nutrition, elevated interstitial fluid pressure and chronic and fluctuating levels of oxygenation [1,2]. The ECM is composed of complex assemblies of collagens, glycosaminoglycans (GAGs), proteoglycans and the molecules that bind to these compoents [3]. Though tumor stromal interaction frequently occurs directly through cadherin-adhesions [4] and indirectly through ECM remodeling [5], tumor cells also dynamically interact with those stromal components through growth factor-mediated tumor-stromal cells crosstalk and integrin-mediated tumor-ECM interactions [6,7]. These interactions modify the surrounding microenvironment to facilitate abnormal growth, angiogenesis, invasion and ultimately metastasis as the disease progresses [8]. In general, tumor growth and progression require intricate interactions between cancer cells and their surrounding microenvironment [9]. Deeply understanding the relationship between the tumor microenvironment and tumor cell behavior is crucial to developing therapeutics that can prevent or control breast tumors.

The matrix stiffness of breast tumor tissue is often increased compared with that of peritumor and normal tissue [10], and this feature plays an important role in processes of cancer progression, including cell proliferation, drug resistance, and reversion to a more invasive phenotype [11,12]. Increasing matrix stiffness may directly induce the epithelial-to-mesenchymal transition (EMT) of certain epithelial tumor cells [13]. To investigate the dynamic cell-cell and cell-tumor microenvironment interactions, the matrix stiffness of cell culture platforms should be tunable. Conventional two-dimensional (2D) platforms suffer from serious limitations given the lack of 3D architecture for suitable growth factor-mediated cell-cell and integrin-mediated cell-matrix interactions *in vivo*. Moreover, the stiffness of 2D culture materials (such as tissue culture polystyrene (TCPS)

Peer review under responsibility of KeAi Communications Co., Ltd.

* Corresponding author. Mechanobiology and Regenerative Medicine Laboratory, Bioengineering College, Chongqing University, 174 Shazheng Street, Shapingba District, Chongqing, 400044, China.
E-mail address: yglv@cqu.edu.cn (Y. Lv).
[1] Web: http://yglvbme.com.

https://doi.org/10.1016/j.bioactmat.2021.02.004
Received 14 September 2020; Received in revised form 25 January 2021; Accepted 5 February 2021

and glass) is of the order of MPa and stiffer than that of human soft tissue (approximately kPa), which could alter the cancer signaling because cellular behavior is widely recognized to be influenced by substrate stiffness [14]. Although animal models can mimic the tumor microenvironment in humans and serve as the gold standard for cancer research, these models contain several uncontrollable factors, such as hemodynamics, immune response and animal individual differences [15,16].

To overcome these disadvantages, many 3D culture models were developed to better mimic the tumor microenvironment and culture tumor cells *in vitro*. Specifically, 3D bioengineered tumor models mainly contain synthetic and natural scaffolds. Synthetic polymers, including poly (ethylene glycol) (PEG) [17], polycaprolactone (PCL) [18], poly (lactic-coglycolic) (PLGA) [19], and synthetic peptides [20], possess good properties of biochemistry and biomechanics, and were specifically designed to replicate the *in vivo* tumor microenvironment [21]. Although the synthetic scaffold can be functionalized with adhesion ligands, like RGD peptide [22], to realize cell adhesion, there is still a limitation for synthetic scaffolds due to the lack of an *in vivo*-like structure and natural components to some extent. In addition, synthetic scaffold degrades rapidly along with the accumulation of acidic degradation products, which may reduce the viability of tumor cells [23]. Studies have reported that biologically derived natural scaffolds, such as basement membrane (Matrigel) [24], collagen [25], and fibrin [26] could promote cell attachment and proliferation but were not able to completely reflect the tumor microenvironment. The elastic modulus of these scaffolds was different from that of tumor tissue, altering signaling and forming various cell morphologies [12]. Moreover, in some specific cases, cancer cells seeded in Matrigel form a spheroid-like construct with diameter of 99 ± 20 μm, which was less than the maximum diffusion limit of oxygen (approximately 150 μm) [27]. A hypoxic core could not be formed in the spheroid but is present in most tumors *in vivo*. Furthermore, specific molecules in the ECM, such as fibrin and collagen, might not be able to simulate the qualitative and quantitative changes in the ECM of primary tumors in a temporal manner. The ECM can regulate the function of the cells and concentration of growth factors and receptors through transduction signaling of cell surface receptors to achieve homeostasis [28]. Decellularized ECM (DECM), as a type of natural substrate, not only maintains the biomechanical characteristics of the primary tumor, but also retains the components and structure of the ECM. Only cells and nucleic acids are removed from this natural substrate, and the ideal microenvironment components for tumors, such as collagen, proteoglycan, laminin, elastin and growth factors, are reserved [29,30]. DECM regulates tissue homeostasis and angiogenesis, morphology, structure, gene expression and cell signaling in a manner that is analogous to cells *in vivo*, thus providing a powerful 3D scaffold for preclinical tumor research [31,32].

In addition to biochemical factors, physical components in the ECM can also regulate the response of cells to the microenvironment and their interactions [33]. In particular, most tumorigenesis was accompanied abnormal ECM deposition and increased stiffness [34]. These features contribute enhance integrin-mediated contacts and increase the expression of focal adhesions and secretion of proteolytic enzymes [35]. The invasive region of the more aggressive tumor subtype exhibits the most heterogeneous matrix, where tumor cells can active macrophages and transforming growth factor-β (TGF-β) mechanics signaling to facilitate ECM remolding [36]. Further research in mice has demonstrated that the elevated expression of collagen can promote breast tumorigenesis and metastasis, and tumor regions are stiffer than the normal tissue [37]. The different tumor stiffness is mainly due to the heavy cross-linking of abundant collagen, a predominant component of the ECM. In particular, lysyl oxidase (LOX), an extracellular matrix-modifying enzyme, is necessary for the stabilization and integrity of the ECM by driving the formation of covalent cross-linking of collagen and elastin [38]. Activated LOX stiffens the tumor tissue, whereas reduced LOX activity can callback the stiffness and prevent tissue fibrosis [39]. During breast tumorigenesis, LOX-mediated collagen cross-linking and tissue stiffening improve integrin aggregation, detect mechanically activated kinase of focal adhesion kinase (FAK) and p130Cas, enhance PI3K activity, and induce integrin-mediated mechanical transduction [40,41]. Increased ECM stiffness has a positive correlation relationship with the concentration, fiber width and cross-linking degree of collagen, and highly metastatic tumor cells have been observed in mammary cancer patients with high levels of cross-linked collagen [42,43]. Moreover, LOX can regulate the metastatic tissue microenvironment during fibrosis to create an environment that is beneficial to tumor cells growth after metastatisis [44]. In general, LOX plays important roles in regulating the process whereby a benign tumor is transformed into an invasive malignant tumor through ECM cross-linking and integration [45].

So, whether *in vitro* 3D tumor scaffolds with appropriate matrix stiffness could be prepared by decellularizing solid tumors originated from MDA-MB-231 cells with different LOX expression are studied. In this study, lentivirus vectors (LV) for LOX interference (IF) and overexpression (OE) were constructed and then separately transfected into human breast cancer MDA-MB-231 cells. LOX mRNA and protein expression was further measured. Furthermore, cells with different LOX expression levels were subcutaneously injected into the nude mouse armpit. Once the tumor tissue formed, a decellularized approach was applied to harvest the 3D DECM scaffolds. The major components, microstructure and elastic modulus of the DECM were characterized. Finally, after recellularization and culture of DECM scaffolds with MDA-MB-231, cell viability, drug resistance to a specific model drug cisplatin (DDP) and the expression levels of some chemoresistance related genes and proteins were verified.

2. Materials and methods

2.1. Constructing LOX overexpression lentivirus (LOX-OE-LV) and LOX interference lentivirus (LOX-IF-LV)

The human LOX gene was identified via a search of a gene database and the sequence was showed in the supplementary for the sequence of LOX gene. The gene has a total of 1254 bp. The siRNA against human LOX gene sequences are as follows: forward, GGA ACU UUA GUG AAA CAU AAU; reverse, UAU GUU UCA CUA AAG UUC CAG. The retrieval of the sequence from the gene database confirmed that siRNA exhibited no homology with any human gene sequences except for LOX.

For LOX gene overexpression, upstream and downstream specific amplification primers were designed and the restriction site was introduced. The specific sequences were amplified by quantitative real-time polymerase chain reaction (qPCR) and then connected to the pCDH green fluorescent protein (pCDH-GFP) plasmid vector. For LOX gene interference, double-stranded DNA oligo interfering sequences were constructed and then inserted into the pGCL-GFP plasmid vector (including U6 promoter). Both products were transfected into bacterial competent cells, separately, and monoclonal colonies were identified through qPCR. The standard for successful construction of LOX-OE-LV and LOX-IF-LV were positive clones. Then, the recombinant virus plasmid and the two supplementary packaged plasmids were extracted with high purity without endotoxin and subsequently used for cotransfection of 293T cells using lipidosome 2000 (Invitrogen, USA). Finally, cell supernatant containing lentivirus particles were collected and concentrated by ultracentrifugation. The titer and multiplicity of infection index (MOI value: the ratio of the number of infectious virus particles to the number of target cells) were examined before transfection.

2.2. Cell culture and transfection

Human invasive breast cancer MDA-MB-231 cells (purchased from the Institute of Biochemistry and Cell Biology, Shanghai Institutes for Biological Sciences, Chinese Academy of Sciences) were cultured in high

glucose Dulbecco's modified Eagle's medium (DMEM) (Gibco, USA) supplemented with 10% fetal bovine serum (FBS) (Gibco, USA), 100 μg/ml antibiotics streptomycin sulfate and 100 U/ml benzyl penicillin. Cells were cultured in 37 °C in a humidified 5% CO_2 incubator and passaged every 3 days. The medium was changed every 2 days.

Three groups were established, including the overexpression group that was transfected with LOX-OE-LV, the interference group that was transfected with LOX-IF-LV, and the blank control group. Briefly, 2×10^5 cells were seeded onto the plastic of six-well plates and incubated for 16–20 h. After the lentivirus vector was dissolved on ice, 60 μl of 1×10^8 TU/ml lentivirus vector and 2 μl polybrene (10 μg/μl, Yeasen, China) were added to 2 ml of culture medium to form a mixed solution. After transfection, cells were screening by puromycin and flow cytometry. When the cell confluence rate was approximately 70% as assessed by a microscope, the mixed solution was added to 6-well plates, and the plates were incubated at 37 °C in a 5% CO_2 humidified atmosphere. GFP expression was observed after incubation for 24, 48, 72 and 96 h.

2.3. qPCR and western blot

Total RNA was extracted using by a Trizol kit (Qiagen, Germany). RNA concentration was quantified by Nanodrop, and 1 μg RNA was used to generate reverse-transcribed complementary DNA (cDNA). cDNA synthesis was performed using a high-capacity cDNA-reverse-transcription kit (Thermo Scientific, USA) per the manufacturer's instruction. qPCR was performed according to the instructions of Quant SYBR Green PCR detection kits (Takara, Japan). Reactions for each sample were performed in triplicate, and amplified products were visualized using a real-time quantitative fluorescence gene amplification device (Bio-Rad, USA). The PCR conditions were 95 °C for 30 s, 95 °C for 5 s, and 60 °C for 30 s for 40 cycles followed by 95 °C for 10 s, 65 °C 5 s, and 95 °C 5 s. The primer sequences are presented in Table S1.

Total protein was extracted using radio-immunoprecipitation assay buffer (RIPA) (Beyotime, China) containing phenylmethanesulfonyl fluoride (PMSF) (Beyotime, China). The samples were then centrifuged at 12000 rpm at 4 °C for 15 min. Protein concentrations were quantified using BCA followed by the separation with 10% sodium dodecyl sulfate polyacrylamide gel electrophoresis (SDS-PAGE) using 60 μg total protein per well. Proteins were then transferred for 2 h at 200 mA to a polyvinylidene difluoride (PVDF) (Bio-Rad, USA) membrane. Membranes were blocked for 1 h with 5% nonfat dry milk (Boster, China) in tris-buffered saline containing 0.1% Tween 20 (TBST). Then, the following primary antibodies were added as indicated: LOX (Abcam, USA) at 1:1000, FAK (Zen Bio, China) at 1:1000, p-FAK (Zen Bio, China) at 1:1000, adenosine triphosphate (ATP)-binding cassette subfamily B member 1 (ABCB1) (Zen Bio, China) at 1:1000, Yes-associated protein (YAP) (Santa Cruz, USA) at 1:2000, p-YAP (Bioss, China) at 1:1000, B-cell lymphoma-2 (Bcl-2) (Bioss, China) at 1:1000, Bcl-2-associated X (Bax) (Bioss, China) at 1:1000, or glyceraldehyde-3-phosphate dehydrogenase (GAPDH) (Abcam, USA) at 1:3000. Blots were incubated at room temperature for 30 min followed by 4 °C overnight. The membranes were subsequently washed thrice with TBST for 5 min and incubated with horseradish peroxidase-conjugated secondary antibodies (Beyotime, China) at 37 °C for 1 h. Membranes were then washed thrice with TBST 10 min and developed with an enhanced chemi-luminescent (ECL) (Thermo Scientific, USA) detection reagent. Western blot images were developed using a digital darkroom image detector (Bio-Rad, USA). Quantitative analysis was performed using ImageJ software (NIH Image, USA), and protein density was normalized to GAPDH.

2.4. Tumor tissue harvest

All animal experimental procedures and protocols were approved by the Animal Care and Use Committee of Chongqing University. Briefly, 3×10^6 MDA-MB-231 cells with different LOX expression levels were trypsinized and resuspended in 100 μl phosphate-buffered saline (PBS) (Beijing Zhongshan Biotechnology, China) and mixed with 100 μl Matrigel (BD, USA). Then, the mixed solution was subcutaneously injected into the left and right armpit of 4- to 6-week-old male BALB/c-nu mice (purchased from Beijing Experimental Animal Centre of the Chinese Academy of Sciences) using an insulin syringe (Braun, Germany). The tumor volumes were measured every week using a Vernier caliper and calculated using the following formula: $V = 0.5\ ab^2$ $V = 12ab2$ (a: major axis; b: minor axis) [46]. Gross and histological examinations were performed, and the 28-day implanted tumor tissue was chosen for further assessment.

2.5. Preparation of tumor DECM

Tumors were retrieved 28 days after implantation, sliced into sheets (approximately 3 mm in thickness) with an operating scalpel and sheared to disks (approximately 10 mm in diameter). Then, the tumor slices were decellularized using the following procedures according to the protocols described by Lv et al. [29]. Briefly, tumor slices were treated in hypotonic tris buffer (10 mM tris, 5 mM ethylene diamine tetraacetic acid (EDTA), pH 8.0) (Solarbio, China) at 0 °C overnight and then incubated in hypertonic tris buffer (50 mM tris, 1 M NaCl, 10 mM EDTA, pH 8.0) at 37 °C for 24 h. Subsequently, the treated tumor slices were incubated in 0.025% (wt/v) trypsin/0.02% (wt/v) EDTA for 30 min followed by 0.5% (v/v) Triton X-100 (Solarbio, China) for 48 h. Finally, the tumor slices were incubated in DNase I (20 U/ml, Solarbio, China) containing $MgCl_2$ (50 mmol/l) for 24 h. With the exception of the step involving hypotonic tris buffer treatment, other steps were conducted under continuous shaking conditions with 70 rpm at 37 °C. The treated samples were sterilized using 70% ethanol and rinsed in PBS. Sterile samples were stored at 4 °C in PBS containing 1% penicillin/streptomycin until use.

2.6. Histology and immunohistochemistry

DECM samples were fixed in 4% paraformaldehyde for at least 24 h, embedded in paraffin, and sectioned into 5 μm slices. Slides cut from the paraffin-embedded samples were processed for histologic and immunohistochemical staining. Prior to staining, sections were dewaxed in xylene and rehydrated using graded industrial denatured alcohol. Slides underwent hematoxylin and eosin (HE) staining (Beyotime, China), Masson trichrome staining (Nanjing Jiancheng Biotechnology, China) and Scott's alcian blue staining (Solarbio, China). Slides were imaged using a fluorescence microscope (Olympus IX71, Japan).

2.7. DNA content assay

To assess total DNA content within native tissue and decellularized matrices, a DNA isolation kit (Solarbio, China) was used according to the manufacturer's manual. Briefly, 20 mg dry samples were digested with Proteinase K (Solarbio, China) overnight. The remaining DNA was diluted with tris EDTA buffer (TE) buffer (10 mM tris-HCl, 1 mM EDTA, pH 8.0). DNA concentrations were calculated using a calf thymus DNA standard curve prepared with 10 ng/μl, 20 ng/μl, 40 ng/μl, and 80 ng/μl and expressed as ng/mg dry tissue weight. Briefly, 10 μl DNA solution was mixed with 90 μl tris sodium chloride EDTA buffer (TNE) (10 mM tris-HCl, 1 mM EDTA, 1 M NaCl) in 96-well plates, and 100 μl Hoechst 33258 (20 μg/ml) was added in every well. Plates were protected from light for 5 min. The test solution was measured using a fluorescence microplate reader (Tecon, USA) at an excitation wavelength of 355 nm and emission wavelength of 462 nm.

2.8. ECM component evaluation

Collagen was detected with the Sirius Red Collagen Detection kit (Chondrex, USA) according to the manufacturer's protocol. Briefly, native tissue and decellularized tumor were cut into pieces and

incubated for 48 h at 4 °C in an acid-pepsin solution (Solarbio, China). Then, 100 μl extracted solution was mixed with 500 μl Sirius Red Solution for 20 min, and the mixture was centrifuged at 10,000 rpm for 3 min. The supernatant was removed, and washing solution was added. After centrifugation, 250 μl extraction buffer was added to the collagen precipitate. The absorbance of the sample was measured at 550 nm, and collagen content was calculated using a standard curve.

GAG content was assayed as previously reported in the literature [29]. Briefly, the samples were treated with 25 mg/ml papain solution (Solarbio, China) (0.1 M NaH_2PO_4, 5 mM EDTA, 5 mM L-Cysteine HCl) at 60 °C for 24 h to extract GAGs. Then, 40 μl extracted solution was mixed with 1 ml dimethylmethylene blue (Sigma, USA). The resulting solution was transferred to a 96 well plate (200 μl/well). The absorbance of the sample was measured at 590 nm, and bovine chondroitin sulfate (Solarbio, China) was calculated using a standard curve.

2.9. Scanning electron microscopy (SEM) detection

DECM samples were frozen at −80 °C and lyophilized for SEM [47]. These dry samples were sputter-coated with gold and examined using SEM (JEOL, Japan) at an accelerating voltage of 5 kV.

2.10. Porosity measurement

The porosities of DECM samples were measured by liquid displacement [48]. Briefly, the lyophilized samples were immersed in a graduated cylinder filled with a known volume (V1) of absolute ethanol, and then the cylinder was placed in vacuum for 30 min to enable complete penetration of ethanol into the pores of the scaffold. The total volume of the sample including ethanol was recorded as V2. The sample was removed from the cylinder, and the volume of residual ethanol was recorded as V3. The porosity (%) was calculated as follows: $[(V1–V3)/(V2–V3)]\times100\%$, where V1–V3 represents the volume of ethanol retained in the sample and V2–V3 represents the total volume of the sample. Ethanol was used because it could easily penetrate into the pores of DECM samples without causing shrinkage or swelling.

2.11. Tissue biomechanical property testing

The uniaxial tensile tests of samples were measured with a material testing machine (Instron, USA). Briefly, the lyophilized samples (6 mm in width and 10 mm in length) used for wet tests were prepared by soaking them in PBS at room temperature for 8 h to achieve a completely swollen state. Then, the prepared samples were stress-loaded at a rate of 0.1 mm/s until rupture. The elastic modulus (E) of the sample was obtained from the linear region of the stress-strain curve for each sample.

2.12. Recellularization

Lyophilized DECM samples were sheared to disks (6 mm in diameter), sterilized using 75% ethanol, rinsed in PBS and rehydrated in culture media overnight. For the 2D culture group, cells were seeded in 48-well plates at 1×10^5 cells in 1 ml fully supplemented DMEM nutrient media per well. For the DECM culture groups, polyhydroxyethylmethacrylate (PHEMA) (Sigma, USA) was added in 48-well plates and then retrieved after slight shake. Plates were rinsed with PBS rinse after the PHEMA was volatilized. The treated DECM samples were placed into the 48-well plates, and 1×10^5 cells in 40 μl culture media were seeded onto each sample and incubated at 37 °C for 2 h. Then, 1 ml fully supplemented DMEM nutrient media containing 1% penicillin-streptomycin and 10% FBS was added to each well for further culture. Cell culture medium was carefully changed every other day.

Cell seeding efficiency (CSE) of MDA-MB-231 cells in the DECM scaffolds with different stiffness was assayed. DNA isolation and quantification were performed according to the procedures described in the 'DNA Content Assay' section. DNA content of the cells in the scaffolds recellularized for 24 h was recorded as $DNA_{scaffold}$, and the DNA content of the initial seeded cells (1×10^5 cells) was recorded as $DNA_{initial}$. The SCE was calculated using the following formula: $DNA_{scaffold}/DNA_{initial}\times100\%$.

The DNA content of MDA-MB-231 cells cultured in the scaffolds for ten days was measured using DNA quantification. A known number of MDA-MB-231 cells (2.5×10^4 cells, 5×10^4 cells, 1×10^5 cells, 2×10^5 cells, 4×10^5 cells) were examined based on DNA quantification to produce a standard curve. The cell number in each sample was calculated from the standard curve.

2.13. Cell viability

The viability of MDA-MB-231 cells cultured on 2D and recellularized samples for 1, 4, 7, and 10 days were quantitatively determined using the 3-(4,5-dimethylthiazol-2-yl)-5-(3-carboxymethoxyphenyl)-2-(4-sulfophenyl)-2H-tetrazolium, inner salt (MTS) assay (Promega, USA). Briefly, 50 μl MTS stock solution mixed with 500 μl DMEM was added to each well and incubated at 37 °C for 2 h. Then, 100 μl of mixed solution was aspirated into 96-well plates with three repetitions per sample.

For live imaging of cultured cells, 2D cultured cells or cells seeded in scaffolds were incubated in PBS containing 1 mM calcein AM (Invitrogen, USA) and 1 mM propidium iodide (PI) (Sigma, USA) at 37 °C for 30 min, rinsed twice with PBS and finally observed with a fluorescence microscope (Olympus IX71, Japan).

2.14. Cell infiltration

To visualize cell infiltration in scaffolds with different stiffness, the scaffolds seeded with MDA-MB-231 cells were fixed in 4% paraformaldehyde for 30 min. After washing with PBS, the samples were incubated with 4′,6-diamidino-2-phenylindole dihydrochloride (DAPI) solution (Solarbio, China) for 10 min and finally observed with laser scanning confocal microscope (Leica TCS SP8, Germany). Moreover, samples recellularized for 1, 4, 7, and 10 days were fixed in 4% paraformaldehyde for 24 h, and the infiltration of tumor cells in the scaffolds was evaluated by HE staining.

2.15. Drug response analysis

MDA-MB-231 cells were cultured in DECM scaffolds with different stiffness for 10 days, whereas cells cultured on the 2D TCPS served as the control. Then, the medium containing DDP (Sigma, USA) was added and treated for 48 h. Cell viability was examined using the MTS assay (Promega, USA) as described above. The IC50 values (concentration for 50% inhibition) were obtained by fitting the cell survival curve using the Boltzmann function in GraphPad Prism 7.0 (GraphPad Software, San Diego, CA).

To inhibit activation of ABCB1 or Bcl-2, MDA-MB-231 cells were cultured in DECM scaffolds for 10 days and then were incubated with 2 μM elacridar (Beyotime, China) or 1 μM ABT-737 (Beyotime, China) for 48 h at 37 °C before being subjected to DDP treatment.

2.16. Flow cytometry

MDA-MB-231 cell apoptosis was analyzed using an Annexin V-FITC/PI apoptosis assay kit (Neobioscience, China). Briefly, cells grown in the DECM scaffolds were harvested with trypsin. Cells were then resuspended in binding buffer and stained with Annexin V-FITC and PI for 15 min at room temperature in the dark. For cell cycle analysis, MDA-MB-231 cells prepared from either 3D cultures (at Day 10) or 2D cultures were treated with cold 75% ethanol at 4 °C overnight. Fixed cells were washed with cooled PBS and incubated with propidium iodide solution (Keygen, China) for 30 min at room temperature. All analyses were performed using a FACS Calibur analyzer (BD Biosciences, USA) with FlowJo software (Tree Star Software, San Carlos, California, USA).

2.17. Statistical analysis

All measurements were collected at least three times. The data were presented as the means ± standard deviation (SD). Data were analyzed using one-way analysis of variance (ANOVA) followed by Tukey's post hoc test with GraphPad Prism 7.0 (GraphPad Software, San Diego, CA). P values < 0.05 were considered statistically significant, and P values < 0.01 were considered extremely statistically significant.

3. Results

3.1. Transfection efficiency

MDA-MB-231 cells were separately transfected with LOX-OE-LV and LOX-IF-LV. Untransfected cells were treated as the control group in which the cells spread evenly and presented spindle and irregular polygonal shapes. More cells in the interference group were characterized by a spindle shape and more cells in the overexpression group were characterized by an irregular polygon shape. GFP expression indicated that the cells were transfected by LOX-OE-LV and LOX-IF-LV with high transfection efficiency (Fig. 1a). Compared to the control group, LOX mRNA and protein expression was significantly inhibited in the interference group ($P < 0.05$) and significantly increased in the overexpression group ($P < 0.01$) (Fig. 1b and c).

3.2. Growth and harvest of tumor tissue

MDA-MB-231 cells with different LOX expression levels were subcutaneously injected into the armpit of nude mice (Fig. 1). As shown in Fig. 1j, the volume of tumor formed from cells with different LOX expression levels showed no significant difference and increased as the implantation time increased, which was approximately 200 mm^3, 500 mm^3, 1000 mm^3, and 2000 mm^3 after implantation for 7 days, 14 days, 21 days, and 28 days, respectively. Tumors retrieved at 28 days post-implantation were chosen for further treatment (Fig. 1i) and exhibited an opaque ellipsoid shape without necrosis, possessing certain elasticity and vascularization (Fig. 1d and e). Then, these tumors were sliced into sheets (approximately 3 mm in thickness) with an operating scalpel and sheared to disks (approximately 10 mm in diameter) (Fig. 1f and g). After decellularization, translucent soft tissues were obtained and their volumes were reduced compared with solid tumor due to complete cell removal (Fig. 1h). The biomechanical properties of DECM scaffolds were measured using an Instron material testing machine (Fig. 1k). According to our hypothesis, cells with high LOX expression form solid tumors with high stiffness and cells with low expression of LOX form solid tumors with low stiffness. The elastic modulus of the DECM scaffold in the Low stiffness group (LSG) (in figures, it was showed as Low) (0.74 ± 0.10 kPa) was significantly reduced compared with the Medium stiffness group (MSG) (in figures, it was showed as Medium) (1.60 ± 0.14 kPa) and the High stiffness group (HSG) (in figures, it was showed as High) (1.99 ± 0.19 kPa) ($P < 0.01$). The elastic modulus of the DECM scaffold

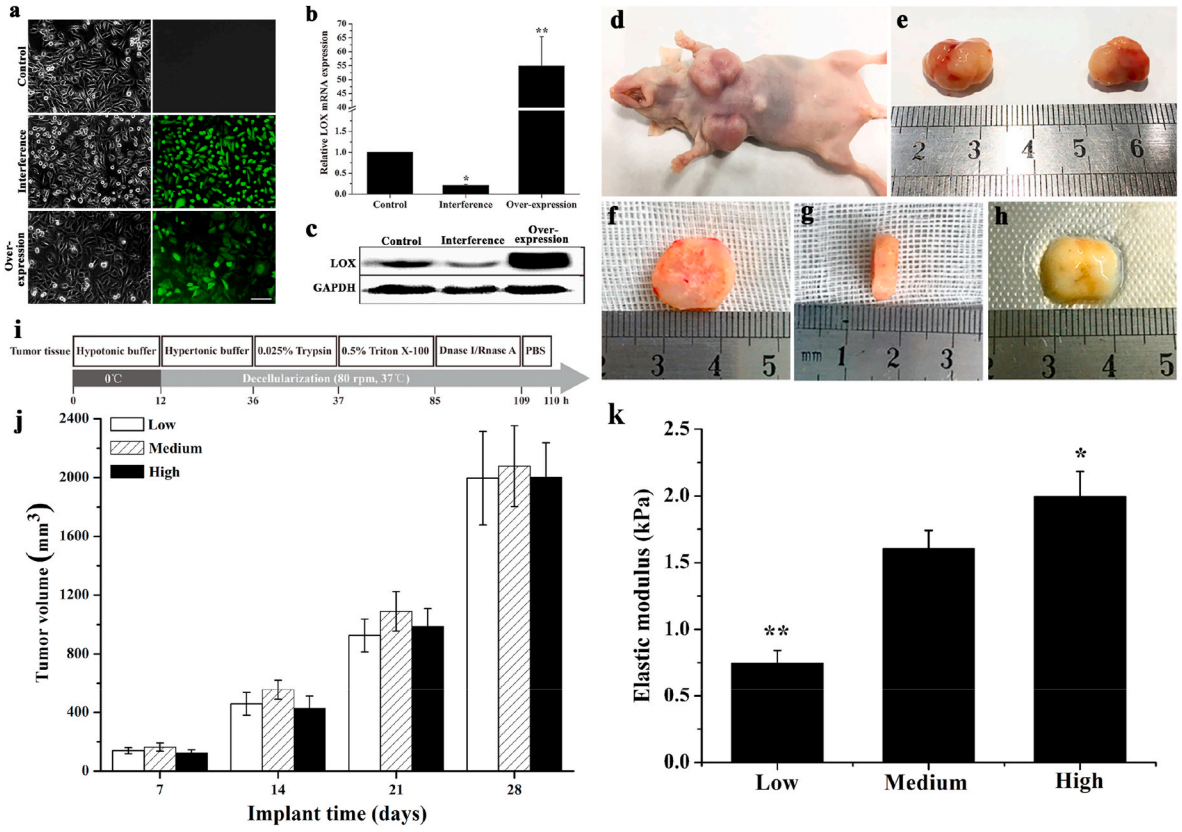

Fig. 1. The generation of MDA-MB-231 cells with different LOX expression levels and harvest of tumor tissue. (a) Morphology and GFP expression of MDA-MB-231 after lentiviral transfection. Left: cell morphology under phase contrast microscope; Right: GFP expression. Scale bar: 100 μm. (b) qPCR analysis of the mRNAs expression level of LOX which was normalized to GAPDH (n = 3, $*P < 0.05$, $**P < 0.01$, compared with the control group, ANOVA followed by Tukey's post hoc test). (c) Western blotting analysis of LOX protein expression of the cells. (d, e) Tumor tissue after subcutaneous injection into the armpit of male nude mice. (f) Diameter of tumor tissue sample. (g) Thickness of tumor tissue sample. (h) Decellularized tumor tissue sample. (i) Schematic illustration of the decellularization procedure. (j) Tumor volumes at different time postimplantation (n = 3). Low: low stiffness group; Medium: medium stiffness group; High: high stiffness group. (k) Elastic modulus of DECM scaffold (n = 3). $*P < 0.05$ represents statistically significant difference compared with the Medium group. $**P < 0.01$ represents extremely statistically significant difference compared with the he Medium group. Statistical significance was determined by ANOVA followed by Tukey's post hoc test. Low: low stiffness group; Medium: medium stiffness group; High: high stiffness group.

in the HSG was significantly increased compared with the MSG ($P < 0.05$).

3.3. Characterization of tumor tissue before and after decellularization

The resultant DECM scaffolds were stained by HE staining to examine residual ECM components. Cell nuclei were observed in native tumor tissues but not in the DECM scaffolds (Fig. 2a), demonstrating the removal of cellular components. Moreover, the ECM density of the HSG was increased compared with the MSG and LSG. Masson trichrome staining and Scott's alcian blue staining also confirmed that cells had been removed while collagen and GAGs were maintained in DECM scaffolds. Increased collagen and GAGs levels were noted in the HSG compared with the MSG and LSG (Fig. 2b and c). However, collagen and GAG assays showed no significant differences among these three groups after decellularization (Fig. 2d and e). After decellularization, the DNA content in the MSG was reduced from 74.61 ± 13.78 ng/mg to 0.91 ± 0.10 ng/mg ($P < 0.01$). In the LSG and HSG, DNA content was also significantly reduced from 76.56 ± 9.45 ng/mg and 66.12 ± 11.30 ng/mg to 0.97 ± 0.15 ng/mg ($P < 0.01$) and 1.07 ± 0.08 ng/mg ($P < 0.01$) after decellularization, respectively (Fig. 2f).

3.4. Characterization of scaffold

SEM revealed that the DECM scaffold of each group has 3D network fibrous structure with evenly distributed holes (Fig. 3a). The porosity in the MSG was 48.47 ± 5.27%, which was significantly lower than that of the LSG (68.12 ± 5.74%), but significantly higher than that of the HSG (32.68 ± 4.30%) (Fig. 3b). The significant difference in porosity among different groups arose from the intensity of cross-linking, which may have important effects on cell proliferation and infiltration during recellularization.

3.5. Recellularization performance of MDA-MB-231 within DECM scaffolds with different stiffness

DNA quantification showed that approximately 3×10^5 cells grew on the scaffolds after recellularization for 10 days and there was no significant difference among these three scaffolds ($P > 0.05$) (Fig. 4a). To evaluate the recellularization performance, the CSE of three groups was measured after recellularization for 24 h. CSE in these three groups was greater than 50% and no obvious differences were noted among these three groups ($P > 0.05$) (Fig. 4b).

To compare the viability profiles under different conditions, MDA-

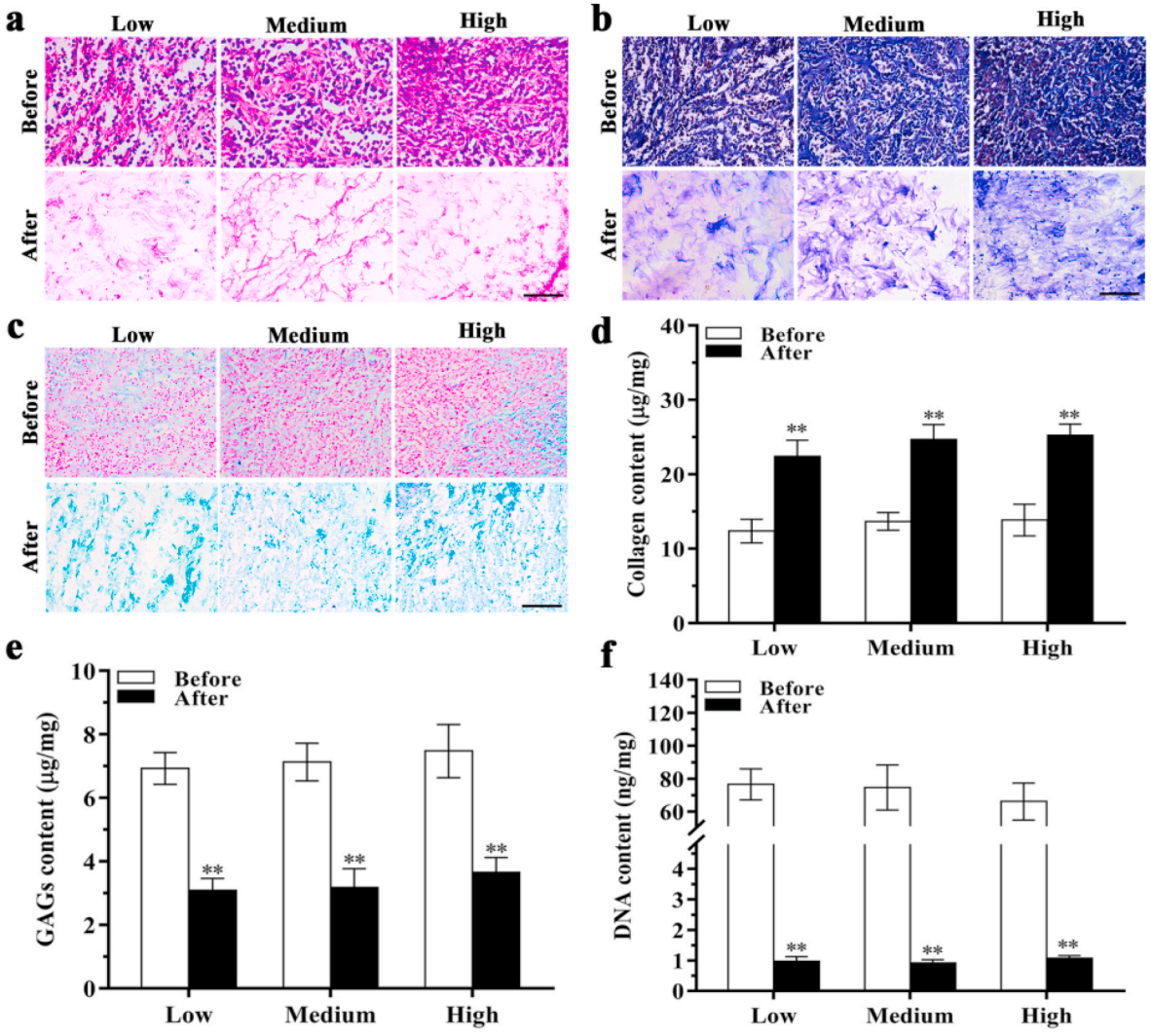

Fig. 2. Characterization of ECM before and after decellularization. (a) HE staining. (b) Masson's trichrome staining. (c) Scott's alcian blue staining. (d) Collagen content analysis (n = 4). (e) GAG content analysis (n = 4). (f) DNA content analysis (n = 3). Scale bar: 50 μm $^{**}P < 0.01$ represents statistically significant difference between before and after decellularization in each group (ANOVA followed by Tukey's post hoc test). Before: before decellularization. After: after decellularization. Low: low stiffness group; Medium: medium stiffness group; High: high stiffness group.

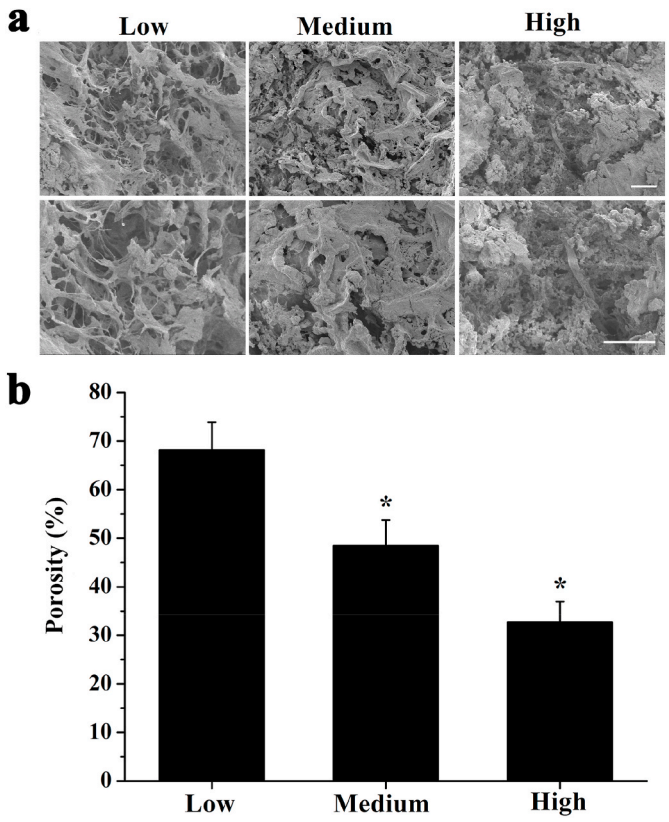

Fig. 3. Microstructural and mechanical characterization of DECM scaffold. (a) SEM examination for DECM scaffold microstructure in each group. Scale bar: 100 μm. (b) Porosity of DECM scaffold in each group (n = 3). *$P < 0.05$ represents statistically significant difference compared with the Low group.

MB-231 cell viability on the TCPS and in the DECM scaffolds was measured by MTS at 1, 4, 7, and 10 days (Fig. 4c). A similar trend in cell viability was noted in both the TCPS and DECM scaffolds, which achieved a peak value after culture for 7 days. The cells exhibited increased viability on the TCPS compared with the 3D DECM scaffolds. However, cell viability in DECM scaffolds with different stiffness exhibited no obvious differences. Live/dead staining was used to further verify cell viability and compatibility (Fig. 4d). On the TCPS, living cells continually increased in culture for 7 days and began to decrease on day 10. In the DECM scaffolds, significantly more living cells were noted at day 7 compared with days 1 and 4. After culture for 10 days, the number of living cells was similar to that noted at day 7, and a few dead cells were observed, which was consistent with the MTS curve presented in Fig. 4c.

HE staining showed that the LSG has larger pores and fewer ECM compared to the MSG and HSG, and the cell infiltration depth in the LSG and MSG increased over time (Fig. 4e). To more vividly observe cell infiltration, 3D cell distribution in the scaffolds was observed by laser scanning confocal microscope on day 7. As shown in Fig. 4f, cells in the HSG and MSG grew to 20–25 μm, while cells in the LSG could spread longitudinally to 30–35 μm. This result is generally consistent with HE staining results. The quantification of maximum migration distance is counted which is shown in Fig. S1.

3.6. Drug resistance of MDA-MB-231 cells in DECM scaffolds with different stiffness

MDA-MB-231 cells were seeded in DECM scaffolds with different stiffness for 10 days and then treated with different concentrations of DDP (5, 10, 20, 40, and 80 μM) for 48 h. Cells cultured on the TCPS served as the control group. The cytotoxicity of DDP to MDA-MB-231 cells cultured on the TCPS and DECM scaffolds with different stiffness is presented in Fig. 5. Cell viability decreased as the DDP concentration increased. When the concentration of DDP was greater than 20 μM, increased cell viability was noted in DECM scaffolds compared with the TCPS (Fig. 5a). IC_{50} values in the MSG and the HSG were increased compared with values obtained on the TCPS and in the LSG (Fig. 5b). As shown in Fig. 5c and d, MDA-MB-231 cells cultured on the TCPS exhibited the highest level of apoptosis after treatment with 20 μM DDP, and this value was significantly higher than those of the DECM scaffolds ($P < 0.05$). Among the DECM scaffolds, the number of apoptotic cells in the MSG and HSG was significantly lower than that in the LSG ($P < 0.01$).

Cell cycle distribution of MDA-MB-231 cells cultured on the TCPS and in the DECM scaffolds was analyzed using flow cytometry. Without DDP treatment (0 μM), only 40.74 ± 6.39% MDA-MB-231 cells on the TCPS were in the G1 phase, and this value was significantly reduced compared with that noted on the DECM scaffolds ($P < 0.05$). After treatment with 20 μM DDP for 48 h, cells on the TCPS and in the LSG and MSG showed obvious G1 arrest, and the number of arrested cells was significantly increased compared with the respective untreated groups ($P < 0.05$) (Fig. 6a and b). After treatment with 20 μM DDP, the percentage of proliferative cells on the TCPS and in the DECM scaffolds significantly decreased ($P < 0.05$), and the percentage of proliferative cells in the HSG (20.18 ± 2.93%) was significantly higher than that in the LSG (13.33 ± 1.45%) ($P < 0.05$) (Fig. 6c). These results showed that high stiffness could increase the drug resistance of MDA-MB-231 cells in the DECM scaffolds.

3.7. Mechanism of drug resistance of MDA-MB-231 cells cultured in the DECM scaffolds with different stiffness

To further understand the mechanism of drug resistance of MDA-MB-231 cells, various chemoresistance markers in MDA-MB-231 cells cultured in DECM scaffolds with different stiffness were analyzed using qPCR and Western blots (Fig. 7). Compared with the LSG and the MSG, the HSG exhibited increased mRNA expression levels of FAK, Bcl-2 and ABCB1 in MDA-MB-231 cells after recellularization and culture in DECM scaffolds for 10 days ($P < 0.05$) (Fig. 7a). The expression of ATP-binding cassette subfamily C member 3 (ABCC3) and ATP-binding cassette transporter G2 (ABCG2) in the DECM scaffolds with different stiffness exhibited no obvious differences ($P > 0.05$). Relative Bcl-2/Bax protein level in the HSG (1.31 ± 0.097) was significantly higher than those in the LSG (0.634 ± 0.073) and TCPS (0.49 ± 0.072). Relative ABCB1 protein level in the HSG was 0.356 ± 0.049, which was significantly higher than that in the LSG 0.223 ± 0.029 ($P < 0.05$). In addition, increased FAK phosphorylation was noted in the HSG (Fig. 7b). These results indicate that high stiffness may increase MDA-MB-231 cell drug resistance by increasing FAK, Bcl-2 and ABCB1 mRNA and protein expression levels.

To further detect the mechanism of drug resistance of MDA-MB-231 cells, MDA-MB-231 cells were seeded in the DECM scaffolds with different stiffness for 10 days and then treated with 2 μM elacridar for 48 h. Expression of ABCB1 protein in MDA-MB-231 cells was detected by Western blot. After 2 μM elacridar treatment, the expression of ABCB1 protein in MDA-MB-231 cells cultured in DECM scaffolds was significantly decreased, and ABCB1 protein expression did not significantly differ among the groups (Fig. 7c and d). Fig. 7e presents the cell viability before and after 2 μM elacridar treatment as measured by MTS. After elacridar treatment, the IC50 value of each group was reduced, and no obvious differences were noted among these groups (Fig. 7f). Upon treatment with 2 μM elacridar, DDP significantly promoted the apoptosis of cells cultured in the HSG, and the number of apoptotic cells was obviously increased from 11.98 ± 2.95% to 48.89 ± 5.48% ($P < 0.01$) (Fig. 7g and h).

The cell cycle distribution of MDA-MB-231 cells cultured in DECM scaffolds with high stiffness was also analyzed using flow cytometry. Under treatment with 2 μM elacridar, MDA-MB-231 cells showed

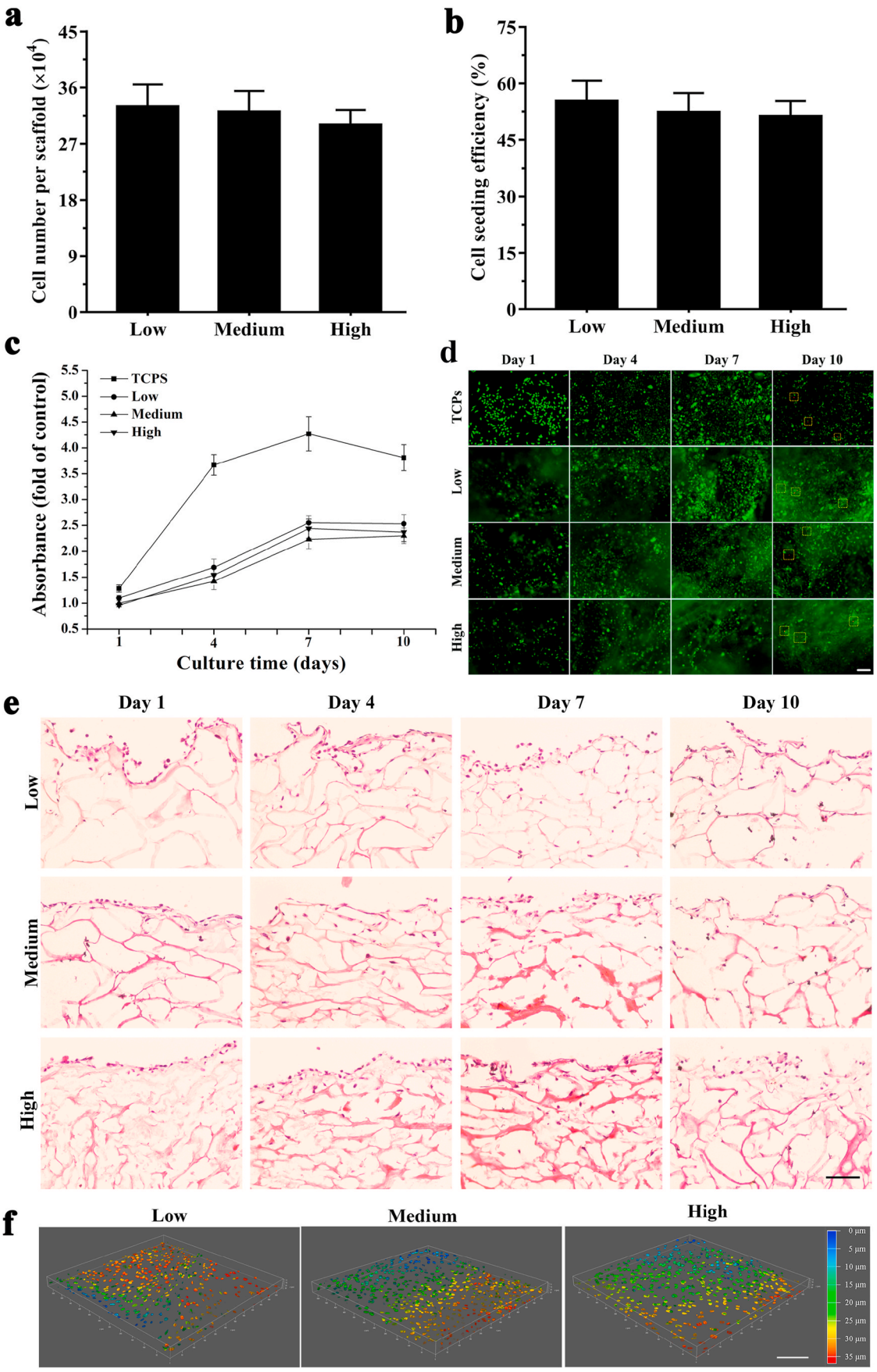

(caption on next page)

Fig. 4. Recellularization performance and cell viability of MDA-MB-231 within DECM scaffolds with different stiffness. (a) CSE of MDA-MB-231 cells in three scaffolds (n = 3). (b) Cell number was detected by quantitative DNA assay for recellularization cultured in the DECM scaffolds with different stiffness at day 10 (n = 3). (c) Cell viability detected by MTS assay for recellularization cultured in the TCPS and DECM scaffolds with different stiffness (n = 3). All the values were normalized to the cell viability on the TCPS at day 1. (d) Cell viability observed by Live/dead staining for recellularization cultured in the TCPS and DECM scaffolds with different stiffness at days 1, 4, 7 and 10. The red square frames identify dead cells. Scale bar: 100 μm. (e) Cell infiltration in DECM with different stiffness was detected by HE staining at days 1, 4, 7 and 10. Scar bar: 50 μm. (f) Cell infiltration in DECM with different stiffness was observed by laser scanning confocal microscope at day 7. Scale bar: 200 μm. Low: low stiffness group; Medium: medium stiffness group; High: high stiffness group.

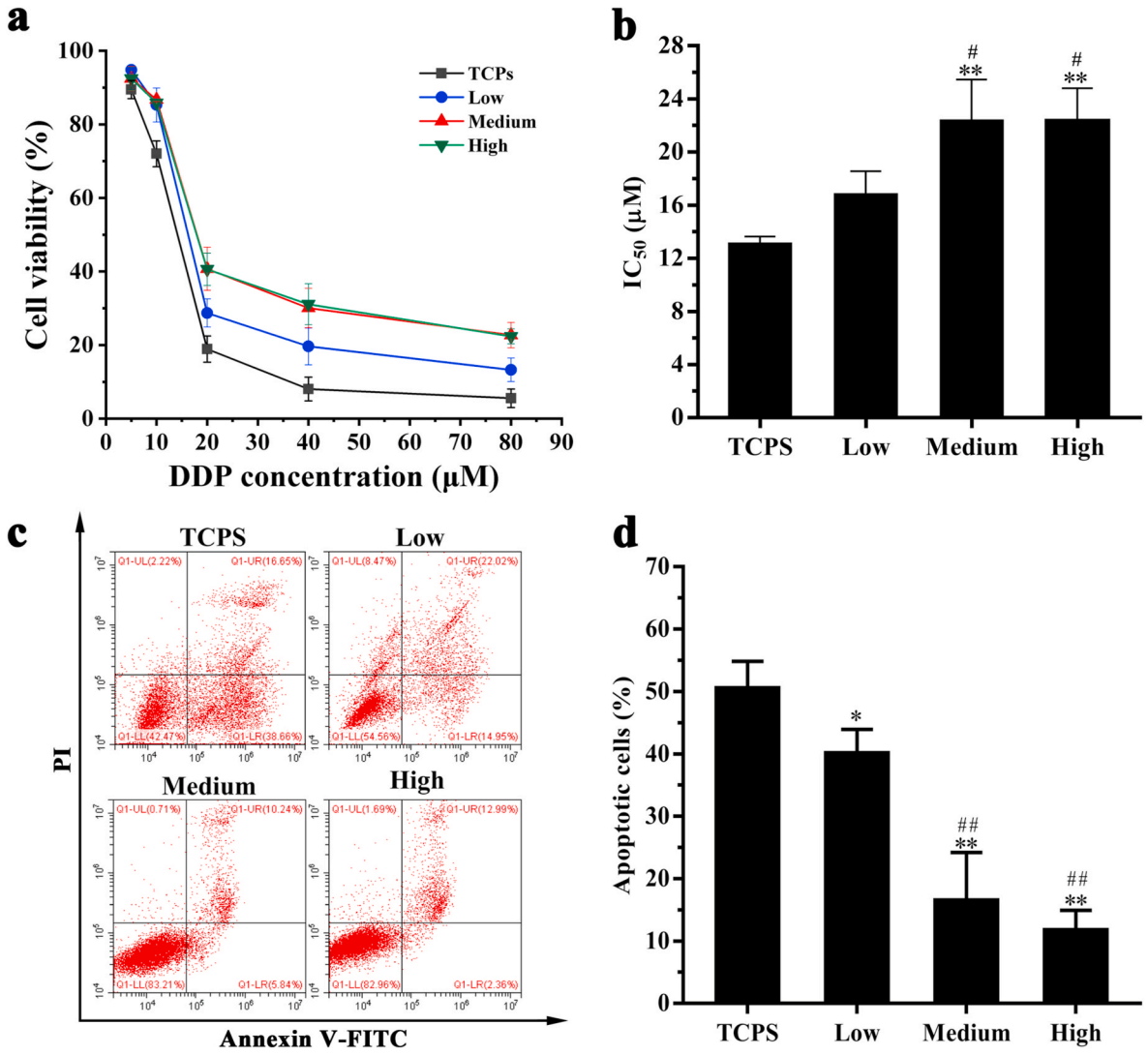

Fig. 5. The cell viability and apoptosis of MDA-MB-231 cells after recellularization for 10 d. (a) Cell viability of MDA-MB-231 cells after treatment with DDP for 48 h (n = 3). (b) IC50 values of DDP for MDA-MB-231 cells. (c) Cell apoptosis of MDA-MB-231 cultured in DECM scaffolds with different stiffness after treated with 20 μM DDP for 48 h. (d) Statistical data of apoptosis (n = 3). $*P < 0.05$ represents statistically significant difference compared with the TCPS group. $**P < 0.01$ represents extremely statistically significant difference compared with the TCPS group. $\#P < 0.05$ represents statistically significant difference compared with the Low group. $\#\#P < 0.01$ represents extremely statistically significant difference compared with the Low group. Statistical significance was determined by ANOVA followed by Tukey's post hoc test. Low: low stiffness group; Medium: medium stiffness group; High: high stiffness group.

significant G1 arrest in the HSG, and these levels were significantly increased compared with cells without elacridar treatment ($P < 0.05$) (Figs. S2a and b). As shown in Fig. S2c, after elacridar drug treatment, the percentage of proliferative cells in the HSG was significantly decreased.

The effect of Bcl-2 on the drug resistance of MDA-MB-231 cells in DECM scaffolds with different stiffness was also assessed in this study (Fig. 8). After 1 μM ABT-737 treatment, the expression of Bcl-2 protein in MDA-MB-231 cells cultured in the HSG was decreased, and no obvious changes were noted in other groups (Fig. 8a and b). The IC_{50} values of each group were reduced (Fig. 8c and d). Upon treatment with 1 μM ABT-737, the number of apoptotic cells increased from 11.98 ± 2.95% to 23.00 ± 2.93% ($P < 0.01$), demonstrating that the DDP significantly promoted MDA-MB-231 cell apoptosis in the HSG (Fig. 8e and f). Furthermore, in contrast to 2 μM elacridar treatment results shown in Figs. S2 and 1 μM ABT-737 treatment did not obviously change the number of cells undergoing G1 arrest in the HSG (Fig. 8g). No significant change in cell proliferation ability was noted in the HSG after treatment with ABT-737 inhibitor (Fig. 8h).

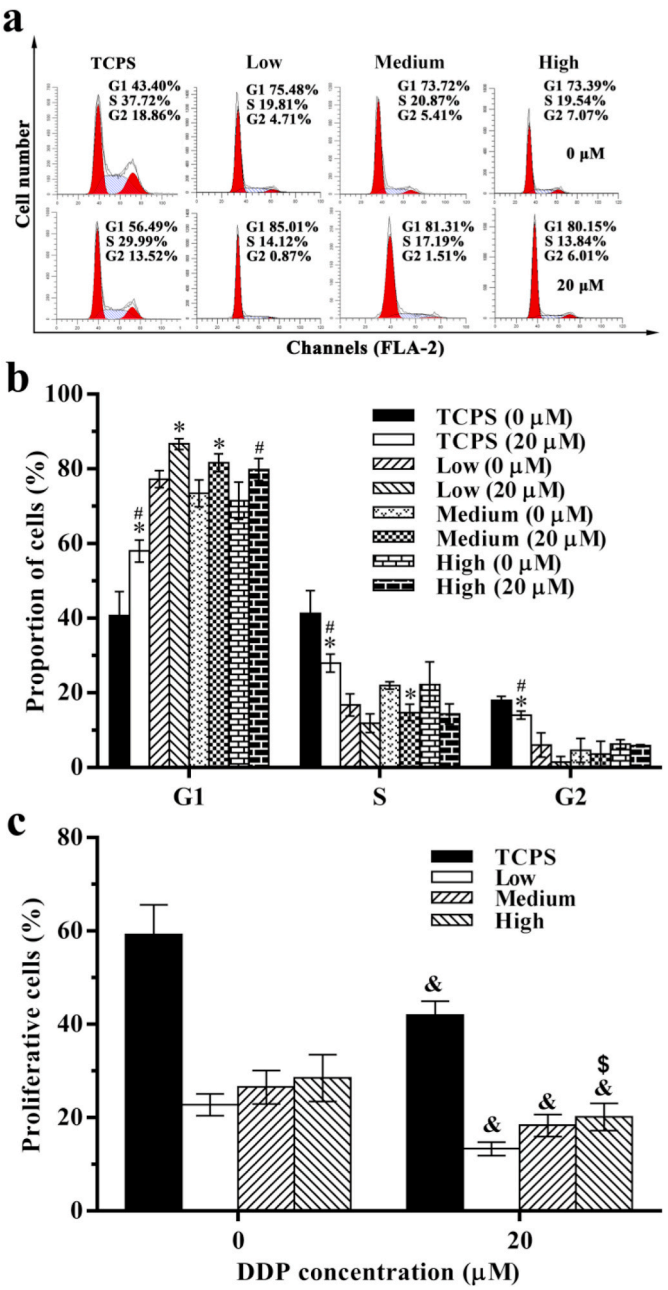

Fig. 6. The cell cycle of MDA-MB-231 cells after recellularization for 10 d. (a) The typical graph of cell cycle. (b) Statistical data of cell cycle (n = 3). (c) Statistical data of cell proliferation (n = 3). *$P < 0.05$ represents statistically significant difference between the DDP treated group and untreated group in the same cell cycle. #$P < 0.05$ represents statistically significant difference compared with the Low group on treated group in the same cell cycle. & $P < 0.05$ represents statistically significant difference between the DDP treated group and untreated group in the same scaffold. $ $P < 0.05$ represents statistically significant difference compared with the Low group after treated with 20 μM DDP. Statistical significance was determined by ANOVA followed by Tukey's post hoc test. Low: low stiffness group; Medium: medium stiffness group; High: high stiffness group.

4. Discussions

In this study, MDA-MB-231 cells with different LOX expression levels were first generated. The target gene or exogenous shRNA were integrated into host gene sequence by LV, thus achieving stable and long-term expression. Our study used LOX-OE-LV and LOX-IF-LV to separately transfect MDA-MB-231 cells. After transfection, cells exhibited altered morphologies and LOX expression of cells. nonuniform GFP expression was noted in the overexpression group (Fig. 1a), which may be due to the lower titer of LOX-OE-LV. However, LOX expression was not affected as shown in Fig. 1b and c. The cell growth status and rate exhibit a tremendous influence on tumor generation. After injection of MDA-MB-231 cells with different LOX expression levels, no significant differences in tumor volumes were noted. Fig. 1 further demonstrates that transfection with LOX-OE-LV and LOX-IF-LV altered cell morphology, but did not affect the cell growth rate. It is reported by previous studies that there is a certain interaction between matrix stiffness and tumor cell growth or proliferation, but it is easy to ignore that the stiffness of material in many of these studies are static, in other words, it cannot changes following with the tumor growth or tumor spheres enlargement [49]. In this present study, the stiffness of solid tumor is realized by the differential expression of LOX. With the growth of tumor, the influence of LOX on the cross-linking degree of ECM collagen also changes, that is, the stiffness of scaffold is dynamic and gradually increases. Therefore, the tumor volume in the three groups is observed to be not so different due to the short time of the tumor formation, which is not very consistent with the results exhibited in the relevant literature. As this study is still in the initial stage, there are certain limitations. So only specific cell lines MDA-MB-231 and commonly used model drugs are selected for drug resistance detection, for which just wishing to explore its feasibility.

In the present work, the solid tumors were harvested by injecting tumor cells in the armpit in male mice. Because the initial purpose of this part of the study was to simply obtain solid tumors, more attention was paid to how to obtain tumors conveniently. Referring to the use of some existing models [50,51], the subaxillary injection was taken out to obtain tumors to meet the experimental assumption without considering the gender of mice. In tumor research, selecting suitable xenograft models is helpful to understand human cell lines and simulate the characteristics of human tumors [52]. According to the transplantation site, it can be classified into orthotopic transplantation and ectopic transplantation. Based on the different experimental purposes, ectopic transplantation can be classified into subcutaneous transplantation which is more flexible for the requirements of inoculation site, tail vein injection for detecting lung metastasis and left ventricular injection for detecting bone and brain metastasis, etc. [53,54]. In addition to the flexible injection site, the enrichment of blood supply in axilla and groin was conducive to the growth of tumor and preferred to be chosen [55]. Fortunately, it can be seen from the results that the tumor obtained by this method has indeed achieved the goal. However, in general, the orthotopic models by using female mice would be more accurate and reasonable, because this model could minimizes the impact of tissue specificity and gender [56]. This is a point worthy of improvement of this study and the related research in the future. On the other hand, nude mice were used in the animal model with injecting subcutaneously human breast tumor cells. The purpose was to reduce the rejection of xenograft cells by immune system in normal mice to immune and inflammatory reactions and avoid the elimination of tumor cells by immune system [57]. Besides the conventional immune response and inflammatory response, such as the normal rejection and clearance of xenograft cells by T cells or inflammatory cells under the regulation of the immune system of recipient animals [58], some host organisms will produce acute rejection or even hyperacute rejection for resistanting the invasion of xenograft cells [59]. For example, guinea pig cells to rat, pig cells to primate, rat cells to mouse and so on, all of which may cause fatal damage to the host animals [60]. At the same time, even if the immunological rejection failed to kill the tumor cells completely or it may cause nonfatal injury to mice [61], it might modify the components of ECM accumulated in the process of tumor progress, of which some specific properties were changed [62]. In addition, in the subcutaneous model of mice with complete immune system, in which mouse tumor cells were transplanted, a human originated tumor could not be formed because of the different origin of tumor cells. Therefore, tumor related

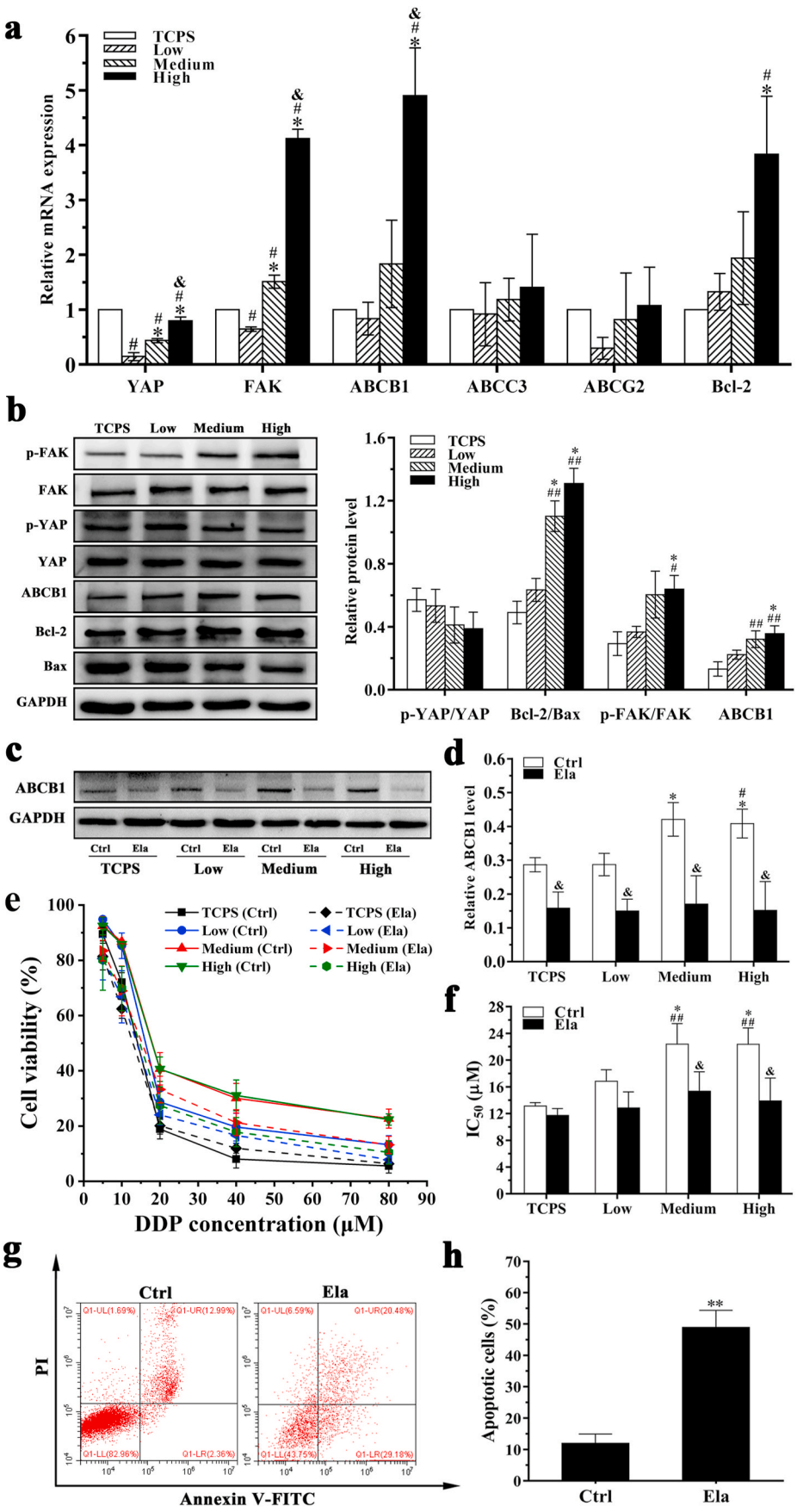

Fig. 7. Effect of ABCB1 on the drug resistance of MDA-MB-231 cells cultured in DECM scaffolds with different stiffness. (a) qPCR analyses for mRNA expression of YAP, FAK, ABCB1, ABCC3, ABCG2 and Bcl-2 which were normalized to GAPDH (n = 3). #$P < 0.05$ represents statistically significant difference compared with the TCPS group; *$P < 0.05$ represents statistically significant difference compared with the Low group. & $P < 0.05$ represents statistically significant difference compared with the Medium group. (b) Western blotting analysis of drug resistance-related proteins expression of the cells (n = 3). #$P < 0.05$ represents statistically significant difference compared with the TCPS group. ##$P < 0.01$ represents extremely statistically significant difference compared with the TCPS group. *$P < 0.05$ represents statistically significant difference compared with the Low group. (c) Western blot detected the expression of ABCB1 protein. (d) Statistical data of the expression of ABCB1 protein (n = 3). *$P < 0.05$ represents statistically significant difference compared with the TCPS group without elacridar treatment. #$P < 0.05$ represents statistically significant difference compared with the Low group without elacridar treatment. & $P < 0.05$ represents statistically significant difference compared with the group without elacridar treatment in the same scaffold. (e) The curve of cell viability. (f) Statistical data of IC50 values (n = 3). ##$P < 0.01$ represents extremely statistically significant difference compared with the TCPS group without elacridar treatment. *$P < 0.05$ represents statistically significant difference compared with the Low group without elacridar treatment. & $P < 0.05$ represents statistically significant difference compared with the group without elacridar treatment in the same scaffold. (g) Cell apoptosis of MDA-MB-231 cultured in the DECM scaffold with high stiffness before and after treated with 2 μM elacridar. (h) Statistical data of apoptosis (n = 3). **$P < 0.01$ represents extremely statistically significant difference compared with the group without elacridar treatment. Statistical significance was determined by ANOVA followed by Tukey's post hoc test. Low: low stiffness group; Medium: medium stiffness group; High: high stiffness group. Ctrl: group without elacridar treatment. Ela: group treated with 2 μM elacridar.

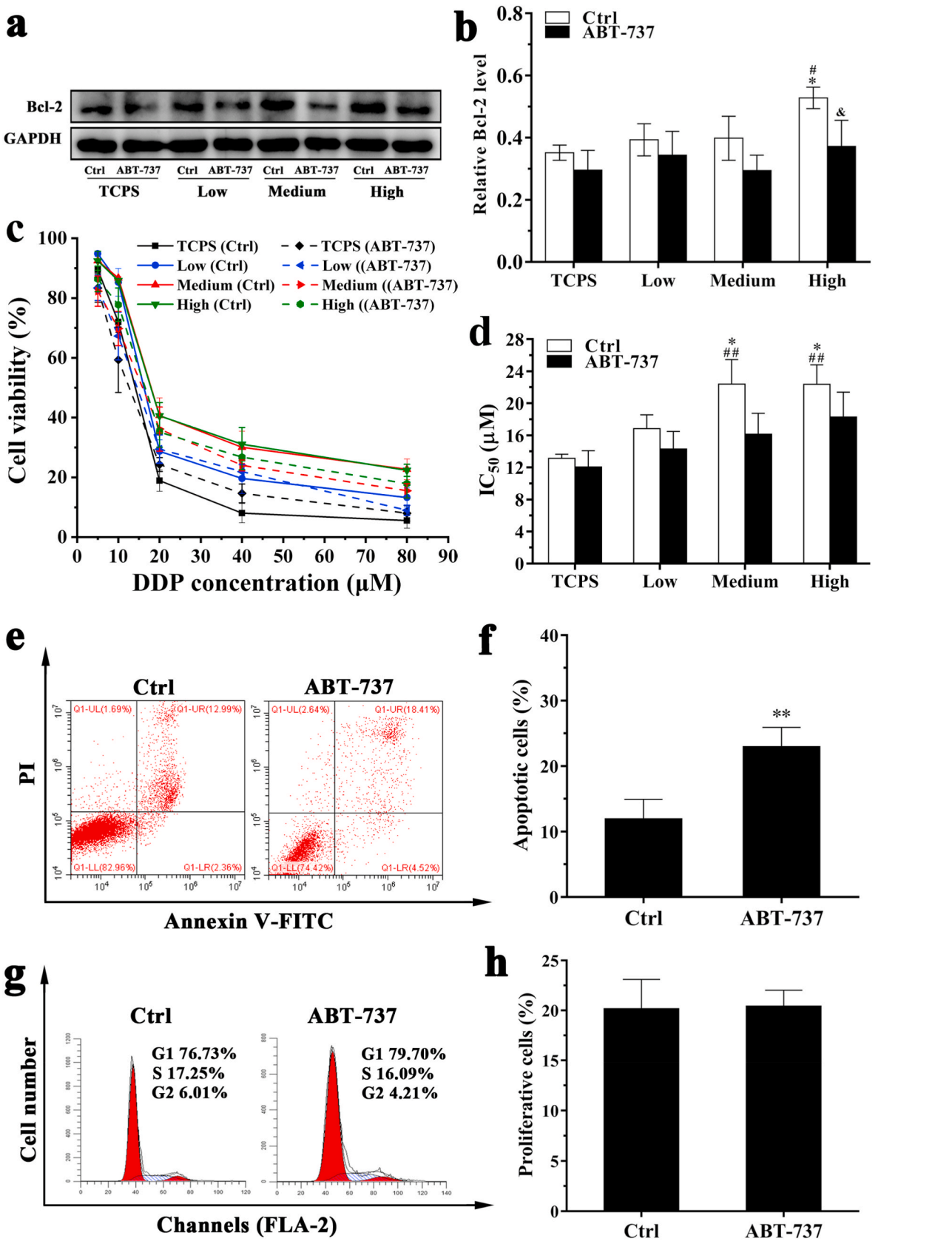

(caption on next page)

Fig. 8. Effect of Bcl-2 on the drug resistance of MDA-MB-231 cells cultured in DECM scaffolds with different stiffness. (a) Western blot detected the expression of Bcl-2 protein, (b) Statistical data of the expression of Bcl-2 protein (n = 3). *$P < 0.05$ represents statistically significant difference compared with the TCPS group without ABT-737 treatment. #$P < 0.05$ represents statistically significant difference compared with the Low group without ABT-737 treatment. & $P < 0.05$ represents statistically significant difference compared with the group without ABT-737 treatment in the same scaffold. (c) The curve of cell viability. (d) Statistical data of IC50 values (n = 3). ##$P < 0.01$ represents extremely statistically significant difference compared to the TCPS group without ABT-737 treatment. *$P < 0.05$ represents statistically significant difference compared with the Low group without ABT-737 treatment. (e) Cell apoptosis of MDA-MB-231 cultured in the DECM scaffold with high stiffness before and after treated with 1 μM ABT-737. (f) Statistical data of apoptosis (n = 3). **$P < 0.01$ represents extremely statistically significant difference compared with the group without ABT-737 treatment. (g) The typical graph of cell cycle. (h) Statistical data of cell proliferation (n = 3). Statistical significance was determined by ANOVA followed by Tukey's post hoc test. Low: low stiffness group; Medium: medium stiffness group; High: high stiffness group. Ctrl: group without ABT-737 treatment.

antigens, ECM factors and other factors were different [63]. Although each factor in the tumor microenvironment may have specific conservation or homology in different species, such as the conserved sequence of coding gene or the specific arrangement or structure of protein molecule, it has interspecific specificity [64,65]. Therefore, it is possible that mouse antigens can not specifically bind to human antibodies, or drugs applied to humans can not cure mouse diseases, let alone explore the pharmacology or molecular mechanism. It is the species specificity that makes the tumors originated from mice may not be conducive to the study of human tumor drug response in this research. Therefore, considering the above factors, it was finally decided that the current model was adopted in this study.

Then, the harvested tumors were decellularized to generate the DECM scaffolds with different stiffness (Figs. 2 and 3). Various decellularized approaches have been used in animal tissues that can enable the production of biological scaffolds with functional and structural ECM components and intact vasculature [66]. Our study used hypotonic tris buffer to fix the intermediate filaments of tumor tissue, and then used hypertonic tris buffer to obtain DNA deprotonation and enhance DNA solubility. Subsequently, this study used trypsin/EDTA to digest trypsin of tissues, inhibit nuclease activity and reduce membrane stability. Finally, cells were completely removed by Triton X-100 and DNase/RNase A via Mg^{2+} catalysis [29]. The decellularized method can completely preserve collagen and elastin to maintain the integrity of the matrix structure. Collagen, a major component in connective tissues and organs, provides the structural stiffness for the ECM. Elastin has high elastic modulus and strong stability and was kept in the ECM because of its insolubility in most decellularized reagents. More importantly, LOX, as a key enzyme in the ECM, can catalyze the covalent cross-linking of collagen and elastin, enhancing the stiffness of the ECM [38]. Histological staining results demonstrated that the ECM components such as collagen and glycosaminoglycan were retained in all groups, in which the ECM was intensively cross-linked in the HSG and sparser spaces were found in the LSG (Fig. 2). SEM examination revealed that the significant difference in porosity in the DECM scaffolds arose from the intensity of cross-linking, which may have important effects on cell proliferation and infiltration during recellularization (Fig. 3).

Matrix stiffness plays a significant role in cell proliferation and differentiation, and is also related to porosity of tissue structure [67]. Moreover, 3D fiber-deposited scaffolds exhibited reduced dynamic stiffness and equilibrium modulus with an increasing porosity [68]. Conversely, Williams et al. [69] found that decellularized arteries exhibited increased stiffness compared with native arteries. Collagen fibers of the adventitia were crimped in native arteries but became uncrimped after decellularization. Uncrimping of the collagen fibers and increasing of fiber mobility were conducive to the increased stiffness. Tumor tissue had different structures from the arteries and the collagen fibers were uncrimped before and after decellularization. In addition, solid tumor exhibited a cell-rich structure, and both tumor cells and mesenchymal cells may increase scaffold stiffness. Therefore, loss of these cells will result in a reduction of stiffness. Indentation-type atomic force microscope results showed that biopsy-wide stiffness values from human breast healthy tissues exhibited a unimodal stiffness distribution of 1.13 ± 0.78 kPa. Benign tissues showed an increased stiffness of 3.68 ± 1.92 kPa. In comparison, trimodal distributions of 0.57 ± 0.16 kPa, 1.99 ± 0.73 kPa and 5.75 ± 1.62 kPa were noted in malignant lesions, and the maximum value attained was 20 kPa [10]. Moreover, the nanomechanical response to tumor progression in MMTV-PyMT mice exhibited a bimodal stiffness distribution with two prominent peaks at 0.45 ± 0.12 kPa and 1.29 ± 0.76 kPa in early cancer. However, in late MMTV-PyMT cancer, gradual stiffening was observed from the core to the periphery with peak values shifting from 0.74 ± 0.26 kPa in the core to 5.51 ± 1.70 kPa at the periphery [10]. In addition, biopsyies of human breast tumor tissue with different densities demonstrated a stiffness at 0.5–1.1 kPa in epithelial tissue and 0.8–1.8 kPa in collagen regions [70]. In this study, DECM stiffness significantly differed from that of the native tumor, given that the different degrees of collagen cross-linking fundamentally resulted in significant differences among these groups. However, the DECM scaffolds in different groups were all in the range of 0.8–1.8 kPa. The significant differences among these groups were attributed to the different degrees of collagen cross-linking. In addition, the stiffness value in the HSG was similar to that noted in late MMTV-PyMT cancer, indicating that the DECM scaffold in the HSG could simulate late cancer lesions (Fig. 3).

This study further evaluated MDA-MB-231 cell viability after DECM scaffolds with different stiffness were obtained. During cell seeding, PHEMA was used to treat 24-well plates to promote cell adherence to the DECM to the greatest extent. Live/dead staining demonstrated that the 3D DECM possessed good cytocompatibility (Fig. 4). Cell viability assays partly reflect the proliferation rate of cultured cells. However, the proliferation rate of MDA-MB-231 cells in 3D DECM scaffolds was considerably reduced compared with 2D monolayer cultures *in vitro*. The *in vitro* 2D culture had sufficient oxygen and nutrients; however in 3D DECM, cells at the center may experience hypoxic conditions, receiving less nutrients and oxygen compared with cells at the periphery [71]. This result was consistent with a previous study demonstrating that MCF-7 cell proliferation was reduced in DECM derived from A549 pulmonary adenocarcinoma cells compared with 2D monolayer cultures [29]. Many studies have found that matrix stiffness could regulate metastatic breast tumor cell viability and metabolic state [72–74]. Given the difference in the densities of collagen cross-linking in the DECM, cell proliferation and migration were simultaneously subjected to the effects of matrix stiffness and porosity. In our study, although there was no significant difference in cell proliferation among DECM scaffolds with different stiffness (Fig. 4), the infiltration depth in the LSG was significantly deeper compared with the MSG and the HSG. The sparse matrix and large porosity in the LSG might facilitate cell spreading and migration (Fig. 4). These results demonstrated that the 3D DECM possessed good cytocompatibility.

Finally, the DECM scaffolds developed in this study were used to examine the effect of matrix stiffness on MDA-MB-231 cell drug resistance to some model drugs. Numerous previous studies indicated that the microenvironment between ECM and tumor cells promotes proliferation, invasion, drug resistance, and malignant behaviors of tumor cells by providing chemical and physical cues [75,76]. Our experimental results showed that compared to 2D culture, the recellularized scaffolds increased MDA-MB-231 cell drug resistance *in vitro* with increased cell viability and reduced apoptosis rates after DDP treatment (Figs. 5 and 6). Moreover, in the DECM scaffolds, MDA-MB-231 cells cultured in the HSG were significantly more resistant to DDP compared to cells cultured

in the LSG. This study is consistent the previous study by Joyce and collages [77], wherein substrate stiffness influenced the responses of MDA-MB-231 cells to doxorubicin and MDA-MB-231 cells grown on stiff substrate were more resistant to the common chemotherapy drug doxorubicin than those cultured on 3D soft substrate. Our study demonstrated that 3D matrix stiffness is involved in the regulation of tumor cell resistance.

To explain the mechanism of drug resistance in our experiment, this study further investigated the expression of various chemoresistance markers (ABCB1, ABCC3 and ABCG2), a transcriptional regulator (YAP), and apoptosis-related factors (FAK and Bcl-2) in DECM scaffolds with different stiffness (Figs. 7 and 8). Chemotherapy is one of the most common therapies against cancer, but it often fails due to the occurrence of multidrug resistance (MDR) during chemotherapy. Overexpression of drug efflux transporters of the ATP-binding cassette (ABC) family is a major cause of MDR [78]. ABCB1 belongs to the family of ABC membrane transporters that decrease intracellular drug concentrations and thus contribute to MDR [79]. Previous studies also found that ABCB1 protein is a major contributor to the development of MDR [80]. Therefore, inhibition of ABCB1 protein expression may be an attractive target for therapeutic intervention in the treatment of cancer. This study found that the HSG could induce ABCB1 overexpression in MDA-MB-231 cells (Fig. 7), and inhibition of ABCB1 expression could significantly reduce stiffness-dependent resistance of MDA-MB-231 cells, suggesting that the HSG significantly promoted drug resistance of MDA-MB-231 cells by inducing ABCB1 overexpression. On the one hand, YAP is a transcriptional regulator that can induce the expression of proliferation- and anti-apoptosis-related genes. YAP is directly regulated by ECM, and tumor cells cultured on stiff ECM exhibit nuclear expression of YAP, which may trigger the EMT and promote drug resistance in tumor cells [77]. In this study, YAP gene expression increased slightly as matrix stiffness increased, while the stiffness difference among DECM scaffolds had not obvious effect on YAP nuclear translocation (Fig. 7 and Fig. S3). On the other hand, tyrosine kinase FAK plays an important role in the regulation of reversion to a more invasive phenotype. Studies have reported that FAK is activated in tumor cells grown on stiff substrates and can synergistically promote cell proliferation in conjunction with the pERK and PI3K kinase pathways. In addition, activation of FAK promotes Bcl-2 expression and inhibits p53 and miR-200 expression, thereby inhibiting tumor cell apoptosis [81,82]. In the present study, the HSG exhibited increased FAK phosphorylation and Bcl-2 expression, which was consistent with previous studies.

5. Conclusions

In summary, this study utilized MDA-MB-231 cells with different LOX expression levels to generate DECM scaffolds with different stiffness. Characterization of the DECM indicated that the scaffolds could closely mimic the microenvironment of the breast tumor, especially the ECM and matrix stiffness. During recellularization, these scaffolds provided a 3D environment to study cell viability and resistance to DDP. MDA-MB-231 cells cultured in DECM scaffolds with high stiffness (1.99 $\pm$ 0.19 kPa) exhibited greater resistance via increased expression of drug resistance-related genes. It is believed that the DECM scaffolds with different stiffness are promising platforms to study the effects of stiffness on the morphology, migration, anticancer drug sensitivity and stemness of tumor cells *in vitro*. Additionally, after recellularization, the scaffolds may be implanted into animal bodies to study immunoreaction, cell recruitment mechanisms, cell metastasis and revascularization *in vivo*, which are important in tumor prevention and therapy.

CRediT authorship contribution statement

Yonggang Lv: Conceptualization, Data curation, Formal analysis, Funding acquisition, Investigation, Methodology, Project administration, Resources, Supervision, Validation, Writing - original draft, Writing - review & editing. **Hongjun Wang:** Data curation, Formal analysis, Investigation, Validation, Writing - original draft. **Gui Li:** Data curation, Formal analysis, Investigation, Validation, Writing - original draft. **Boyuan Zhao:** Formal analysis, Writing - review & editing.

CRediT authorship contribution statement

Yonggang Lv: Conceptualization, Data curation, Formal analysis, Funding acquisition, Investigation, Methodology, Project administration, Resources, Supervision, Validation, Writing - original draftWriting – original draft, Writing - review & editingWriting – review & editing. **Hongjun Wang:** Data curation, Formal analysis, Investigation, Validation, Writing - original draftWriting – original draft. **Gui Li:** Data curation, Formal analysis, Investigation, Validation, Writing - original draftWriting – original draft. **Boyuan Zhao:** Formal analysis, Writing - review & editingWriting – review & editing.

Declaration of competing interest

The authors declare no conflict of interests.

Acknowledgments

This work was supported in part by grants from the National Natural Science Foundation of China (11872134, 12072054) and Natural Science Foundation of Chongqing, China (cstc2020jcyj-msxmX0035).

Appendix A. Supplementary data

Supplementary data to this article can be found online at https://doi.org/10.1016/j.bioactmat.2021.02.004.

References

[1] M.E. Rodriguez-Ruiz, I. Vitale, K.J. Harrington, I. Melero, L. Galluzzi, Immunological impact of cell death signaling driven by radiation on the tumor microenvironment, Nat. Immunol. 21 (2020) 120–134, https://doi.org/10.1038/s41590-019-0561-4.

[2] B. Mlecnik, G. Bindea, A. Kirilovsky, H.K. Angell, A.C. Obenauf, M. Tosolini, S. E. Church, P. Maby, A. Vasaturo, M. Angelova, T. Fredriksen, S. Mauger, M. Waldner, A. Berger, M.R. Speicher, F. Pagès, V. Valge-Archer, J. Galon, The tumor microenvironment and immunoscore are critical determinants of dissemination to distant metastasis, Sci. Transl. Med. 8 (327) (2016), https://doi.org/10.1126/scitranslmed.aad6352, 327ra26.

[3] R.K. Jain, Delivery of molecular and cellular medicine to solid tumors, Adv. Drug Deliv. Rev. 64 (1–3) (2012) 353–365, https://doi.org/10.1016/s0169-409x(00)00131-9.

[4] Y. Attieh, A.G. Clark, C. Grass, S. Richon, M. Pocard, P. Mariani, N. Elkhatib, T. Betz, B. Gurchenkov, D.M. Vignjevic, Cancer-associated fibroblasts lead tumor invasion through integrin-β3-dependent fibronectin assembly, J. Cell Biol. 216 (11) (2017) 3509–3520. https://doi: 10.1083/jcb.201702033.

[5] E.C. Costa, A.F. Moreira, D. de Melo-Diogo, V.M. Gaspar, M.P. Carvalho, I. J. Correia, 3D tumor spheroids: an overview on the tools and techniques used for their analysis, Biotechnol. Adv. 34 (8) (2016) 1427–1441. https://doi: 10.1016/j.biotechadv.2016.11.002.

[6] T. Murata, H. Mizushima, I. Chinen, H. Moribe, S. Yagi, R.M. Hoffman, T. Kimura, K. Yoshino, Y. Ueda, T. Enomoto, E. Mekada, HB-EGF and PDGF mediate reciprocal interactions of carcinoma cells with cancer-associated fibroblasts to support progression of uterine cervical cancers, Canc. Res. 71 (21) (2011) 6633–6642, https://doi.org/10.1158/0008-5472.can-11-0034.

[7] J.S. Desgrosellier, D.A. Cheresh, Integrins in cancer: biological implications and therapeutic opportunities, Nat. Rev. Canc. 10 (1) (2010) 9–22, https://doi.org/10.1038/nrc2748.

[8] D.F. Quail, J.A. Joyce, Microenvironmental regulation of tumor progression and metastasism, Nat. Med. 19 (11) (2013) 1423–1437, https://doi.org/10.1038/nm.3394.

[9] M. Stadler, S. Walter, A. Walzl, N. Kramer, C. Unger, M. Scherzer, D. Unterleuthner, M. Hengstschläger, G. Krupitza, H. Dolznig, Increased complexity in carcinomas: analyzing and modeling the interaction of human cancer cells with their microenvironment, Semin. Canc. Biol. 35 (2015) 107–124, https://doi.org/10.1016/j.semcancer.2015.08.007.

[10] M. Plodinec, M. Loparic, C.A. Monnier, E.C. Obermann, R. Zanetti-Dallenbach, P. Oertle, H.J.T. yotyla1, U. Aebi, M. Bentires-Alj, R.Y.H. Lim, C. Schoenenberger,

The nanomechanical signature of breast cancer, Nat. Nanotechnol. 7 (11) (2012) 757–765, https://doi.org/10.1038/nnano.2012.167.
[11] J.Y. Lee, J.K. Chang, A.A. Dominguez, H. Lee, S. Nam, J. Chang, S. Varma, L.S. Qi, R.B. West, O. Chaudhuri, YAP-independent mechanotransduction drives breast cancer progression, Nat. Commun. 10 (1) (2019) 1848, https://doi.org/10.1038/s41467-019-09755-0.
[12] T. Panciera, A. Citron, D.D. Biagio, G. Battilana, A. Gandin, S. Giulitti, M. Forcato, S. Bicciato, V. Panzetta, S. Fusco, L. Azzolin, A. Totaro, A.P.D. Tos, M. Fassan, V. Vindigni, F. Bassetto, A. Rosato, G. Brusatin, M. Cordenonsi, S. Piccolo, Reprogramming normal cells into tumour precursors requires ECM stiffness and oncogene-mediated changes of cell mechanical properties, Nat. Mater. 19 (7) (2020) 797–806, https://doi.org/10.1038/s41563-020-0615-x.
[13] M.G. Ondeck, A. Kumar, J.K. Placone, C.M. Plunkett, B.F. Matte, K.C. Wong, L. Fattet, J. Yang, A.J. Engler, Dynamically stiffened matrix promotes malignant transformation of mammary epithelial cells via collective mechanical signaling, Proc. Natl. Acad. Sci. U.S.A. 116 (9) (2019) 3502–3507, https://doi.org/10.1073/pnas.1814204116.
[14] S.C. Wei, L. Fattet, J.H. Tsai, Y. Guo, V.H. Pai, H.E. Majeski, A.C. Chen, R.L. Sah, S. S. Taylor, A.J. Engler, J. Yang, Matrix stiffness drives epithelial-mesenchymal transition and tumour metastasis through a TWIST1-G3BP2 mechanotransduction pathway, Nat. Cell Biol. 17 (5) (2015) 678–688, https://doi.org/10.1038/ncb3157.
[15] G. Rijal, W.A. Li, Versatile 3D tissue matrix scaffold system for tumor modeling and drug screening, Sci. Adv. 3 (9) (2017), e17080764, https://doi.org/10.1126/sciadv.1700764.
[16] V. Brancato, J.M. Oliveira, V.M. Correlo, R.L. Reis, S.C. Kundu, Could 3D models of cancer enhance drug screening? Biomaterials 232 (2020) 119744, https://doi.org/10.1016/j.biomaterials.2019.119744.
[17] X. Yi, D. Zhao, Q. Zhang, J. Xu, G. Yuan, R. Zhuo, F. Li, Preparation of multilocation reduction-sensitive core crosslinked folate-PEG-coated micelles for rapid release of doxorubicin and tariquidar to overcome drug resistance, Nanotechnology 28 (8) (2017), 085603, https://doi.org/10.1088/1361-6528/aa5715.
[18] E.L.S. Fong, S. Lamhamedi-Cherradi, E. Burdett, V. Ramamoorthy, A.J. Lazar, F. K. Kasper, M.C. Farach-Carson, D. Vishwamitra, E.G. Demicco, B.A. Menegaz, H. M. Amin, A.G. Mikos, J.A. Ludwig, Modeling ewing sarcoma tumors *in vitro* with 3D scaffolds, Proc. Natl. Acad. Sci. U.S.A. 110 (6) (2013) 6500–6505, https://doi.org/10.1073/pnas.1221403110.
[19] J. Wu, C. Deng, F. Meng, J. Zhang, H. Sun, Z. Zhong, Hyaluronic acid coated PLGA nanoparticulate docetaxel effectively targets and suppresses orthotopic human lung cancer, J. Contr. Release 259 (2017) 76–82, https://doi.org/10.1016/j.jconrel.2016.12.024.
[20] S. Dissanayake, W.A. Denny, S. Gamage, V. Sarojini, Recent developments in anticancer drug delivery using cell penetrating and tumor targeting peptides, J. Contr. Release 250 (2017) 62–76, https://doi.org/10.1016/j.jconrel.2017.02.006.
[21] D.W. Hutmacher, Biomaterials offer cancer research the third dimension, Nat. Mater. 9 (2) (2010) 90–93, https://doi.org/10.1038/nmat2619.
[22] W.Y. Wang, C.D. Davidson, D. Lin, B.M. Baker, Actomyosin contractility-dependent matrix stretch and recoil induces rapid cell migration, Nat. Commun. 10 (1) (2019) 1186. https://doi: 10.1038/s41467-019-09121-0.
[23] H.J. Sung, C. Meredith, C. Johnson, Z.S. Galis, The effect of scaffold degradation rate on three-dimensional cell growth and angiogenesis, Biomaterials 25 (26) (2004) 5735–5742, https://doi.org/10.1016/j.biomaterials.2004.01.066.
[24] K.J. Price, A. Tsykin, K.M. Giles, R.T. Sladic, M.R. Epis, R. Ganss, G.J. Goodall, P. J. Leedman, Matrigel basement membrane matrix influences expression of microRNAs in cancer cell lines, Biochem. Biophys. Res. Commun. 427 (2) (2012) 343–348, https://doi.org/10.1016/j.bbrc.2012.09.059.
[25] D. Rodenhizer, E. Gaude, D. Cojocari, R. Mahadevan, C. Frezza, B.G. Wouters, A. P. McGuigan, A three-dimensional engineered tumour for spatial snapshot analysis of cell metabolism and phenotype in hypoxic gradients, Nat. Mater. 15 (2) (2016) 227–234, https://doi.org/10.1038/nmat4482.
[26] L.P. Yan, J.S. ilva-Correia, V.P. Ribeiro, V. Miranda-Gonçalves, C. Correia, A. S. Morais, R.A. Sousa, R.M. Reis, A.L. Oliveira, J.M. Oliveira, R.L. Reis, Tumor growth suppression induced by biomimetic silk fibroin hydrogels, Sci. Rep. 6 (2016) 31037, https://doi.org/10.1038/srep31037.
[27] R. Kerbel, J. Folkman, Clinical translation of angiogenesis inhibitors, Nat. Rev. Canc. 10 (2002) 727–739, https://doi.org/10.1038/nrc905.
[28] C. Fischbach, R. Chen, T. Matsumoto, T. Schmelzle, J.S. Brugge, P.J. Polverini, D. J. Mooney, Engineering tumors with 3D scaffolds, Nat. Methods 4 (10) (2007) 855–860, https://doi.org/10.1038/nmeth1085.
[29] W.D. Lü, L. Zhang, C.L. Wu, Z.G. Liu, G.Y. Lei, J. Liu, W. Gao, Y.R. Hu, Development of an acellular tumor extracellular matrix as a three-dimensional scaffold for tumor engineering, PLoS One 9 (7) (2014), e103672, https://doi.org/10.1371/journal.pone.0103672.
[30] G. Rijal, W. Li, A versatile 3D tissue matrix scaffold system for tumor modeling and drug screening, Sci. Adv. 13 (9) (2017), e1700764, https://doi.org/10.1126/sciadv.1700764.
[31] X. Tian, M.E. Werner, K.C. Roche, A.D. Hanson, H.P. Foote, S.K. Yu, S.B. Warner, J. A. Copp, H. Lara, E.L. Wauthier, J.M. Caster, L.E. Herring, L. Zhang, J.E. Tepper, D. S. Hsu, T. Zhang, L.M. Reid, A.Z. Wang, Organ-specific metastases obtained by culturing colorectal cancer cells on tissue-specific decellularized scaffolds, Nat. Biomed. Eng. 2 (6) (2018) 443–452, https://doi.org/10.1038/s41551-018-0231-0.
[32] B.R. Alabi, R. LaRanger, J.W. Shay, Decellularized mice colons as models to study the contribution of the extracellular matrix to cell behavior and colon cancer progression, Acta Biomater. 100 (2019) 213–222, https://doi.org/10.1016/j.actbio.2019.09.033.
[33] C. Bonnans, J. Chou, Z. Werb, Remodelling the extracellular matrix in development and disease, Nat. Rev. Mol. Cell Biol. 15 (12) (2014) 786–801, https://doi.org/10.1038/nrm3904.
[34] J.I. Lopez, I. Kang, W.K. You, D.M. McDonald, V.M. Weaver, In situ force mapping of mammary gland transformation, Integr. Biol. (Camb.) 3 (2011) 910–921.
[35] M.L. Taddei, E. Giannoni, G. Comito, P. Chiarugi, Microenvironment and tumor cell plasticity: an easy way out, Canc. Lett. 341 (1) (2013) 80–96, https://doi.org/10.1016/j.canlet.2013.01.042.
[36] I. Acerbi, L. Cassereau, I. Dean, Q. Shi, A. Au, C. Park, Y.Y. Chen, J. Liphardt, E. S. Hwang, V.M. Weaver, Human breast cancer invasion and aggression correlates with ECM Stiffening and immune cell infiltration, Integr. Biol. (Camb.) 7 (10) (2015) 1120–1134, https://doi.org/10.1039/c5ib00040h.
[37] P.P. Provenzano, D.R. Inman, K.W. Eliceiri, J.G. Knittel, L. Yan, C.T. Rueden, J. G. White, P.J. Keely, Collagen density promotes mammary tumor initiation and progression, BMC Med. 6 (2008) 11, https://doi.org/10.1186/1741-7015-6-11.
[38] A.M. Baker, D. Bird, J.C. Welti, M. Gourlaouen, G. Lang, G.I. Murray, A. R. Reynolds, T.R. Cox, J.T. Erler, Lysyl oxidase plays a critical role in endothelial cell stimulation to drive tumor angiogenesis, Canc. Res. 73 (2) (2013) 583–594, https://doi.org/10.1158/0008-5472.can-12-2447.
[39] H.E. Barker, T.R. Cox, J.T. Erler, The rationale for targeting the LOX family in cancer, Nat. Rev. Canc. 12 (8) (2012) 540–552, https://doi.org/10.1038/nrc3319.
[40] J.T. Erler, K.L. Bennewith, T.R. Cox, G. Lang, D. Bird, A. Koong, Q.T. Le, A. J. Giaccia, Hypoxia-induced lysyl oxidase is a critical mediator of bone marrow cell recruitment to form the premetastatic niche, Canc. Cell 15 (1) (2009) 35–44, https://doi.org/10.1016/j.ccr.2008.11.012.
[41] D. Barkan, A.F. Chambers, β1-integrin: a potential therapeutic target in the battle against cancer recurrence, Clin. Canc. Res. 17 (23) (2011) 7219–7223, https://doi.org/10.1158/1078-0432.ccr-11-0642.
[42] J.T. Erler, A.J. Giaccia, Lysyl oxidase mediates hypoxic control of metastasis, Canc. Res. 66 (21) (2006) 10238–10241, https://doi.org/10.1158/0008-5472.can-06-3197.
[43] G.L. Semenza, Cancer-stromal cell interactions mediated by hypoxia-inducible factors promote angiogenesis, lymphangiogenesis, and metastasis, Oncogene 32 (35) (2013) 4057–4063, https://doi.org/10.1038/onc.2012.578.
[44] T.R. Cox, D. Bird, A.M. Baker, H.E. Barker, M.W. Ho, G. Lang, J.T. Erler, LOX-mediated collagen crosslinking is responsible for fibrosis-enhanced metastasis, Canc. Res. 73 (2013) 1721–1732, https://doi.org/10.1158/0008-5472.can-12-2233.
[45] M.A. Taylor, J.D. Amin, D.A. Kirschmann, W.P. Schiemann, Lysyl oxidase contributes to mechanotransduction-mediated regulation of transforming growth factor-β signaling in breast cancer cells, Neoplasia 13 (5) (2011) 406–418, https://doi.org/10.1593/neo.101086.
[46] Y. Yoshii, T. Furukawa, A. Waki, H. Okuyama, M. Inoue, M. Itoh, M.R. Zhang, H. Wakizaka, C. Sogawa, Y. Kiyono, H. Yoshii, Y. Fujibayashi, T. Saga, High-throughput screening with nanoimprinting 3D culture for efficient drug development by mimicking the tumor environment, Biomaterials 51 (2015) 278–289, https://doi.org/10.1016/j.biomaterials.2015.02.008.
[47] L. Wang, J.A. Johnson, D.W. Chang, Q. Zhang, Decellularized musculofascial extracellular matrix for tissue engineering, Biomaterials 34 (11) (2013) 2641–2654. https://linkinghub.elsevier.com/retrieve/pii/S014296121300029X.
[48] L. Wang, W.S. Kisaalita, Characterization of micropatterned nanofibrous scaffolds for neural network activity readout for high-throughput screening, J. Biomed. Mater. Res. B Appl. Biomater. 94 (1) (2010) 238–249, https://doi.org/10.1002/jbm.b.31646.
[49] T. Bertero, W.M. Oldham, E.M. Grasset, I. Bourget, E. Boulter, S. Pisano, P. Hofman, F. Bellvert, G. Meneguzzi, D.V. Bulavin, S. Estrach, C.C. Feral, S. Y. Chan, A. Bozec, C. Gaggioli, Tumor-stroma mechanics coordinate amino acid availability to sustain tumor growth and malignancy, Cell Metabol. 29 (1) (2019) 124–140, e10, https://doi: 10.1016/j.cmet.2018.09.012.
[50] P. Yu, R. Wu, Z. Zhou, X. Zhang, R. Wang, X. Wang, S. Lin, J. Wang, L. Lv, rAj-Tspin, a novel recombinant peptide from *Apostichopus japonicus*, suppresses the proliferation, migration, and invasion of BEL-7402 cells via a mechanism associated with the ITGB1-FAK-AKT pathway, Invest. N. Drugs (2020) in press, https://doi: 10.1007/s10637-020-01008-y.
[51] Q. Yang, W.W. Du, N. Wu, W. Yang, F.M. Awan, L. Fang, J. Ma, X. Li, Y. Zeng, Z. Yang, J. Dong, A. Khorshidi, B.B. Yang, A circular RNA promotes tumorigenesis by inducing c-myc nuclear translocation, Cell Death Differ. 24 (9) (2017) 1609–1620. https://doi: 10.1038/cdd.2017.86.
[52] M. Porru, L. Pompili, C. Caruso, C. Leonetti, Xenograft as *in vivo* experimental model, Methods Mol. Biol. 1692 (2018) 97–105. https://doi: 10.1007/978-1-4939-7401-6_9.
[53] C. Khanna, K. Hunter, Modeling metastasis *in vivo*, Carcinogenesis 26 (3) (2005) 513–523. https://doi: 10.1093/carcin/bgh261.
[54] D.X. Nguyen, P.D. Bos, J. Massagué, Metastasis: from dissemination to organ-specific colonization, Nat. Rev. Canc. 9 (4) (2009) 274–284. https://doi: 10.1038/nrc2622.
[55] X. Li, J. Zheng, H. Diao, Y. Liu, RUNX3 is down-regulated in glioma by Myc-regulated miR-4295, J. Cell Mol. Med. 20 (3) (2016) 518–525. https://doi: 10.1111/jcmm.12736.
[56] L. Pudelko, S. Edwards, M. Balan, D. Nyqvist, J. Al-Saadi, J. Dittmer, I. Almlöf, T. Helleday, L. Bräutigam, An orthotopic glioblastoma animal model suitable for high-throughput screenings, Neuro Oncol. 20 (11) (2018) 1475–1484. https://doi: 10.1093/neuonc/noy071.

[57] T. Lu, B. Yang, R. Wang, C. Qin, Xenotransplantation: current status in preclinical research, Front. Immunol. 10 (2020) 3060. https://doi: 10.3389/fimmu.2019.03060.
[58] G.G. MacPherson, S.E. Christmas, The role of the macrophage in cardiac allograft rejection in the rat, Immunol. Rev. 77 (1984) 143–166. https://doi: 10.1111/j.1600-065x.1984.tb00720.x.
[59] R.B. Stevens, J.L. Platt, The pathogenesis of hyperacute xenograft rejection, Am. J. Kidney Dis. 20 (4) (1992) 414–421. https://doi: 10.1016/s0272-6386(12)70310-4.
[60] Z. Zhang, E. Bédard, Y. Luo, H. Wang, S. Deng, D. Kelvin, R. Zhong, Animal model in xenotransplanation, Expet Opin. Invest. Drugs 9 (9) (2000) 2051–2068. https://doi: 10.1517/13543784.9.9.2051.
[61] D.W. Talmage, The acceptance and rejection of immunological concepts, Annu. Rev. Immunol. 4 (1986) 1–11. https://doi: 10.1146/annurev.iy.04.040186.000245.
[62] L. Sorokin, The impact of the extracellular matrix on inflammation, Nat. Rev. Immunol. 10 (10) (2010) 712–723. https://doi: 10.1038/nri2852.
[63] U. Ben-David, G. Ha, Y.Y. Tseng, N.F. Greenwald, C. Oh, J. Shih, J.M. McFarland, B. Wong, J.S. Boehm, R. Beroukhim, T.R. Golub, Patient-derived xenografts undergo mouse-specific tumor evolution, Nat. Genet. 49 (11) (2017) 1567–1575. https://doi: 10.1038/ng.3967.
[64] M. Camacho-Sanchez, P. Burraco, I. Gomez-Mestre, J.A. Leonard, Preservation of RNA and DNA from mammal samples under field conditions, Mol. Ecol. Resour. 13 (4) (2013) 663–673. https://doi: 10.1111/1755-0998.12108.
[65] M.H. Schaefer, J.S. Yang, L. Serrano, C. Kiel, Protein conservation and variation suggest mechanisms of cell type-specific modulation of signaling pathways, PLoS Comput. Biol. 10 (6) (2014), e1003659. https://doi: 10.1371/journal.pcbi.1003659.
[66] J.E. Arenas-Herrera, I.K. Ko, A. Atala, J.J. Yoo, Decellularization for whole organ bioengineering, Biomed. Mater. 8 (1) (2013), 014106, https://doi.org/10.1088/1748-6041/8/1/014106.
[67] K.R. Levental, H. Yu, M.L. Kass, J.N. Lakins, M. Egeblad, J.T. Erler, S.F. Fong, K. Csiszar, A. Giaccia, W. Weninger, M.Y. amauchi, D.L. Gasser, V.M. Weaver, Matrix crosslinking forces tumor progression by enhaning integrin signaling, Cell 139 (5) (2009) 891–906, https://doi.org/10.1016/j.cell.2009.10.027.
[68] L. Moroni, J.R.D. Wijn, C.A.V. Blitterswijk, 3D fiber-deposited scaffolds for tissue engineering: influence of pores geometry and architecture on dynamic mechanical properties, Biomaterials 27 (7) (2006) 974–985, https://doi.org/10.1016/j.biomaterials.2005.07.023.
[69] C. Williams, J. Liao, E.M. Joyce, B. Wang, J.B. Leach, M.S. Sacks, J.Y. Wong, Altered structural and mechanical properties in decellularized rabbit carotid arteries, Acta Biomater. 5 (4) (2009) 993–1005, https://doi.org/10.1016/j.actbio.2008.11.028.
[70] Q. Cheng, C.C. Bilgin, G. Fontenay, H. Chang, M. Henderson, J. Han, B. Parvin, Stiffness of the microenvironment upregulates ERBB2 expression in 3D cultures of MCF10A within the range of mammographic density, Sci. Rep. 6 (2016) 28987, https://doi.org/10.1038/srep28987.
[71] M.B. Meads, R.A. Gatenby, W.S. Dalton, Environment-mediated drug resistance: a major contributor to minimal residual disease, Nat. Rev. Canc. 9 (9) (2009) 665–674, https://doi.org/10.1038/nrc2714.
[72] X. Zhang, L. Yang, S. Chien, Y. Lv, Suspension state promotes metastasis of breast cancer cells by up-regulating cyclooxygenase-2, Theranostics 8 (14) (2018) 3722–3736, https://doi.org/10.7150/thno.25434.
[73] M. Cavo, M. Fato, L. P eñuela, F. Beltrame, R. Raiteri, S. Scaglione, Microenvironment complexity and matrix stiffness regulate breast cancer cell activity in a 3D *in vitro* model, Sci. Rep. 6 (2016) 35367, https://doi.org/10.1038/srep35367.
[74] R.W. Tilghman, C.R. Cowan, J.D. Mih, Y. Koryakina, D. Gioeli, J.K. Slack-Davis, B. R. Blackman, D.J. T schumperlin, J.T. Parsons, Matrix rigidity regulates cancer cell growth and cellular phenotype, PLoS One 5 (9) (2010), e12905, https://doi.org/10.1371/journal.pone.0012905.
[75] S. Hinderer, S.L. Layland, K. Schenke-Layland, ECM and ECM-like materials-biomaterials for applications in regenerative medicine and cancer therapy, Adv. Drug Deliv. Rev. 97 (2016) 260–269, https://doi.org/10.1016/j.addr.2015.11.019.
[76] S. Kumar, R. Kulkarni, S. Sen, Cell motility and ECM proteolysis regulate tumor growth and tumor relapse by altering the fraction of cancer stem cells and their spatial scattering, Phys. Biol. 13 (3) (2016), 036001, https://doi.org/10.1088/1478-3975/13/3/036001.
[77] M.H. Joyce, C. Lu, E.R. James, R. Hegab, S.C. Allen, L.J. Suggs, A. Brock, Phenotypic basis for matrix stiffness-dependent chemoresistance of breast cancer cells to doxorubicin, Front. Oncol 8 (2018) 337, https://doi.org/10.3389/fonc.2018.00337.
[78] W. Li, H. Zhang, Y.G. Assaraf, K. Zhao, X. Xu, J. Xie, D.H. Yang, Z.S. Chen, Overcoming ABC transporter-mediated multidrug resistance: molecular mechanisms and novel therapeutic drug strategies, Drug Resist. Updates 27 (2016) 14–29, https://doi.org/10.1016/j.drup.2016.05.001.
[79] A.K. Nanayakkara, C.A. Follit, G. Chen, N.S. Williams, P.D. Vogel, J.G. Wise, Targeted inhibitors of P-glycoprotein increase chemotherapeutic-induced mortality of multidrug resistant tumor cells, Sci. Rep. 8 (1) (2018) 967, https://doi.org/10.1038/s41598-018-19325-x.
[80] H. Sato, S. Siddig, M. Uzu, S. Suzuki, Y. Nomura, T. Kashiba, K. Gushimiyagi, Y. Sekine, T. Uehara, Y. Arano, K. Yamaura, K. Ueno, Elacridar enhances the cytotoxic effects of sunitinib and prevents multidrug resistance in renal carcinoma cells, Eur. J. Pharmacol. 746 (2015) 258–266, https://doi.org/10.1016/j.ejphar.2014.11.021.
[81] K. Ren, X. Lu, N. Yao, Y. Chen, A. Yang, H. Chen, J. Zhang, S. Wu, X. Shi, C. Wang, X. Sun, Focal adhesion kinase overexpression and its impact on human osteosarcoma, Oncotarget 6 (31) (2015) 31085–31103, https://doi.org/10.18632/oncotarget.5044.
[82] P.J. Keely, Mechanisms by which the extracellular matrix and integrin signaling act to regulate the switch between tumor suppression and tumor promotion, J. Mammary Gland Biol. Neoplasia 16 (3) (2011) 205–219, https://doi.org/10.1007/s10911-011-9226-0.